



Feigenbaum universality in subcritical Taylor–Couette flow

B. Wang¹ , R. Ayats¹ , K. Deguchi² , A. Meseguer³  and F. Mellibovsky³ 

¹Institute of Science and Technology Austria (ISTA), Klosterneuburg 3400, Austria

²School of Mathematics, Monash University, VIC 3800, Australia

³Departament de Física, Universitat Politècnica de Catalunya, Barcelona 08034, Spain

Corresponding authors: K. Deguchi, kengo.deguchi@monash.edu; F. Mellibovsky, fernando.mellibovsky@upc.edu

(Received 24 July 2024; revised 9 January 2025; accepted 2 March 2025)

Feigenbaum universality is shown to occur in subcritical shear flows. Our testing ground is the counter-rotation regime of the Taylor–Couette flow, where numerical calculations are performed within a small periodic domain. The accurate computation of up to the seventh period-doubling bifurcation, assisted by a purposely defined Poincaré section, has enabled us to reproduce the two Feigenbaum universal constants with unprecedented accuracy in a fluid flow problem. We have further devised a method to predict the bifurcation diagram up to the accumulation point of the cascade based on the detailed inspection of just the first few period-doubling bifurcations. Remarkably, the method is applicable beyond the accumulation point, with predictions remaining valid, in a statistical sense, for the chaotic dynamics that follows.

Key words: Taylor-Couette flow, transition to turbulence, chaos

1. Introduction

The Taylor–Couette flow, driven by two independently rotating coaxial cylinders ([figure 1a](#)), has been a prominent research topic in fluid dynamics for over a century. By varying the angular velocities of the cylinders in experimental set-ups, a rich variety of flow patterns can be observed, as documented by Andereck, Liu & Swinney (1986). In this paper, we focus on the case with counter-rotating cylinders, a regime for which Taylor–Couette flow has long served as a paradigm of subcritical transition to turbulence. The onset of fully developed turbulence is preceded by intermittency, with the flow

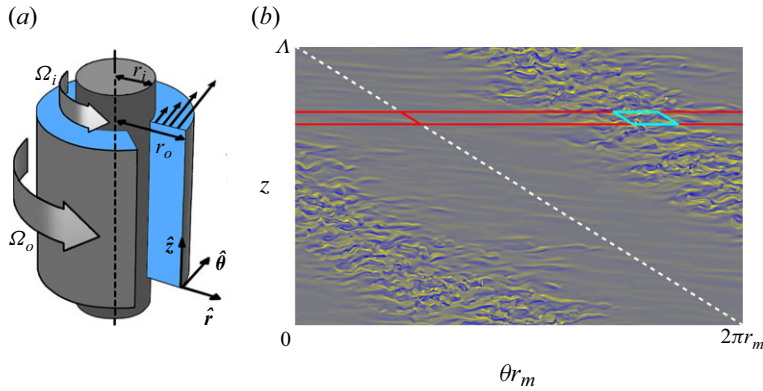


Figure 1. Taylor–Couette flow. (a) Sketch of the flow configuration. The inner and outer cylinders have radii $r = r_i$ and $r = r_o$, respectively, and rotate with angular velocities Ω_i and Ω_o . (b) A snapshot of the stripe pattern adopted from figure 2 of Wang *et al.* (2022). The colour map shows the radial vorticity at the mid gap $r_m = (r_o + r_i)/2$. The radius ratio and inner and outer cylinder Reynolds numbers, defined in § 2, are set to $(\eta, R_i, R_o) = (0.883, 600, -1200)$.

typically exhibiting alternating laminar and turbulent helical bands (Coles 1965; Dong 2009; Meseguer *et al.* 2009b); see figure 1(b).

The mean flow topology of these helical bands (Wang *et al.* 2023) has recently been shown to resemble the laminar–turbulent stripe pattern observed in plane Couette flow (Barkley & Tuckerman 2007). Indeed, large-scale intermittent patterns of coexisting turbulent and laminar regions are ubiquitous in wall-bounded subcritical shear flows (Tuckerman, Chantry & Barkley 2020). Stochastic approaches, such as directed percolation theory, are gaining popularity as a framework for understanding the onset of subcritical turbulent transition (Hof 2023). However, applying stochastic arguments to a deterministic system inherently assumes the pre-existence of chaotic dynamics. In the case of subcritical shear flows, identifying the emergence of chaos that precedes turbulent transition poses a significant challenge.

What complicates the detailed understanding of transitional and fully developed turbulence in shear flows, with all the subtle features it encompasses, is the multi-scale nature of the flow. Consequently, many aspects of subcritical parallel shear flow turbulence have historically been approached using small periodic computational domains called minimal flow units (Jiménez & Moin 1991; Hamilton, Kim & Waleffe 1995; Kawahara, Uhlmann & van Veen 2012). In Taylor–Couette flow, the use of minimal boxes has been common since the early stages of simulations (e.g. Marcus 1984; Coughlin & Marcus 1992). However, most studies employed parameters in the supercritical regime, and somewhat surprisingly, research in the subcritical regime remains rare. A recent review paper (Feldmann *et al.* 2023) hypothesised a connection between subcritical Taylor–Couette flow and plane Couette flow, for which Kreilos & Eckhardt (2012) reported a period-doubling cascade leading to chaos in a small periodic box. Here, we confirm that a period-doubling route to chaos does indeed occur in Taylor–Couette flow within the parameter range studied by Meseguer *et al.* (2009b), Deguchi, Meseguer & Mellibovsky (2014) and Wang *et al.* (2022), the latter hereafter abbreviated as W22.

The most suitable flow unit for the parameter regime we address here is of annular-parallelogram shape proposed by Deguchi & Altmeyer (2013). W22 first used a narrow elongated domain (red box in figure 1b) to compute turbulent stripes in their minimal natural box, a strategy that has been repeatedly adopted in plane Couette

System	Type	n	δ_n		Ref.
Thermal convection	E	4	4.3	± 0.8	Giglio <i>et al.</i> (1981)
Thermal convection	E	4	4.4	± 0.1	Libchaber <i>et al.</i> (1982)
Thermosolutal convection	N (2-D)	3	5	$\pm ?$	Moore <i>et al.</i> (1983)
Taylor–Couette (tilted lid)	E	3	4.67	$\pm ?$	Buzug <i>et al.</i> (1993)
Baffled channels	E and N (2-D)	3	4.65	$\pm ?$	Roberts & Mackley (1996)
Thermal convection	N (2-D)	2	4.9104	$\pm ?$	Lizée & Alexander (1997)
Triple periodic box	N (3-D)	2	4.88	± 0.5	Van Veen (2005)
Thermal convection	N (3-D)	4	4.321	$\pm ?$	Gao <i>et al.</i> (2015)
Forced oscillating cylinder	N (2-D)	5	4.52	$\pm ?$	Cheng <i>et al.</i> (2020)
MHD spherical couette	N (3-D)	4	4.62	$\pm ?$	Garcia <i>et al.</i> (2021)

Table 1. Feigenbaum universality analyses in fluid systems. The table includes the number of period doubling bifurcations analysed (n), and the experimental (E) or numerical (N) nature of the study. An approximation to Feigenbaum’s first constant, estimated from the last three period-doubling bifurcations analysed in each case, is given in column δ_n .

(Barkley & Tuckerman 2007) and channel flows (Tuckerman *et al.* 2014). The domain was subsequently shortened in the azimuthal direction (cyan box in figure 1*b*) so as to fit only one streamwise wavelength of a typical coherent structure of developed turbulence. As reported by W22, the use of such a domain was instrumental in observing the first few period-doubling bifurcations in the route to chaos. In this paper, we show that the ensuing period-doubling cascade aligns exceptionally well with Feigenbaum universality (Feigenbaum 1978, 1979, 1980, 1982).

1.1. Feigenbaum cascade in fluid flows

Feigenbaum universality became widely recognised among fluid dynamicists following the natural convection experiment conducted by Libchaber, Laroche & Fauve (1982), which led to the first empirical approximation of Feigenbaum’s first constant, $\delta_F \approx 4.6692016$, corresponding to the limiting ratio of a period-doubling bifurcation interval to the next (see also the recent article by Libchaber (2023)). Their value, $\delta_4 = 4.4 \pm 0.1$, estimated from up to the fourth period-doubling bifurcation point (hence the subscript $n = 4$), was not too distant from the theoretical value δ_F . Buzug, von Stamm & Pfister (1993) found an estimate close to δ_F when studying a Taylor–Couette apparatus with a tilted lid, while subsequent experimental efforts, summarised in table 1, resulted in persistently larger discrepancies. Estimates compatible with Feigenbaum’s first universal constant have also been obtained numerically for various fluid systems. Some of the values reported for δ_n , also listed in table 1, are reasonably close to δ_F at first glance. However, it must be borne in mind that the reliability of the approximations depends strongly on the number of consecutive period-doubling bifurcations analysed and is extremely sensitive to the accuracy with which they are located. Unfortunately, the approximate determinations of δ_F we have found in the literature of fluid flows were not accompanied with a detailed analysis as done, for example, for the Kuramoto–Sivashinsky equation (Smyrlis & Papageorgiou 1991). Accordingly, their reliability is debatable, as concluding Feigenbaum universality from a handful of period-doubled solutions is, at the very least, perilous.

All the studies presented in table 1 explore period-doubling cascades that follow from a supercritical sequence of bifurcations of the base laminar flow. We focus instead on the subcritical regime, where turbulent transition may occur despite the linear stability of the base flow and can only be triggered by finite amplitude perturbations. The detection and study of period-doubling bifurcations emanating from unstable solutions is impracticable,

and stable finite-amplitude solutions in the subcritical regime of shear flows that could potentially originate a cascade are rare and hard to find. The aforementioned study by Kreilos & Eckhardt (2012) was the first to show that period-doubling cascades may also occur in subcritical transition problems. Their approach consisted in selecting the smallest possible periodic domain that is capable of sustaining turbulence in plane Couette flow while, at the same time, imposing specific discrete symmetries to further constrain the dynamics. Unfortunately, the resolution of their parametric exploration was insufficient to positively confirm universality. Symmetry restrictions were also employed by Moore *et al.* (1983) and Van Veen (2005) in their respective works. A similar period-doubling cascade in plane Couette flow has also been reported in a more recent paper by Lustro *et al.* (2019). However, calculation of δ_F in the subcritical regime of fluid flow problems has not been conducted to date.

1.2. Mathematical aspects of the Feigenbaum cascade

Although period-doubling cascades have been known to occur for over a century (Collet 2019), universality was not discovered until much later by Feigenbaum (1978) and Couillet & Tresser (1978) independently, hence its being often referred to as Feigenbaum–Couillet–Tresser universality by mathematicians. The existence of universality swiftly spread throughout the mathematical community, as vividly depicted by Khanin *et al.* (2021). Since its unveiling, universality has been repeatedly observed in numerical simulations of low-dimensional systems of ordinary differential equations. Checking universality in low-dimensional models like the Rössler system or the Duffing equation has become a common academic exercise. Feigenbaum universality was originally established within the framework of discrete dynamical systems based on one-dimensional iterated maps of the form $x_{\ell+1} = f(x_\ell)$, $\ell \in \mathbb{N}$, with $f(x)$ a unimodal function. Its necessary occurrence in continuous time dynamical systems is typically justified by the use of Poincaré sections. The phenomenon is often illustrated by initially replacing the Smale horseshoe that occurs on the Poincaré section with a Hénon map, which reduces to the logistic map in the limiting case of vanishing area contraction rate after one mapping. Then, since the logistic map is a unimodal map, universality of the period-doubling cascade can be explained by means of renormalisation theory, as done in many standard textbooks such as those by Collet & Eckmann (1980), Schuster (1988), Glendinning (1994) or Strogatz (2024). Universality shows in both the parameter (coordinate) and state (ordinate) axes of the bifurcation diagram, the scaling in the latter axis is related to Feigenbaum’s second constant, $\alpha_F \approx -2.5029079$. In renormalisation theory, α_F and the Feigenbaum function G uniquely solve the Feigenbaum–Cvitanović functional equation $\mathcal{R}[G] = G$ (Feigenbaum 1978; Cvitanović 1989), with the condition $G(0) = 1$. Here, the action of the renormalisation operator, \mathcal{R} , on a function f consists merely in the twice repeated application of f , mediated by a rescaling that involves a factor α_F :

$$\mathcal{R}[f](x) = \alpha_F f \left(f \left(\frac{x}{\alpha_F} \right) \right). \quad (1.1)$$

Despite its simplicity, this operator lies at the heart of the various instances of self-similarity that arise in the bifurcation diagram of the map generated by f . Likewise, Feigenbaum’s first constant δ_F is the leading eigenvalue of the linearisation around G of the renormalisation operator \mathcal{R} , and Φ is the associated eigenfunction (Lanford III 1982; Epstein 1986; Eckmann & Wittwer 1987; Briggs 1991; Stephenson & Wang 1991), which has recently been dubbed Feigenfunction by Thurlby (2021), as a tribute to Feigenbaum. The first mathematical proof of the existence of the universal constants, δ_F and α_F , and functions, G and Φ , is attributed to Lanford III (1982).

Ascertaining universality from the ability to reproduce δ_F and α_F in fluid flow problems presents a twofold challenge. First, a numerical analysis analogous to that of low-dimensional models demands significantly higher computational resources when dealing with the Navier–Stokes equations. The first observation of δ_F in the field of computational fluid mechanics was contributed by Moore *et al.* (1983) when analysing two-dimensional thermosolutal convection. It took, however, until Van Veen (2005) to expose universality in a three-dimensional set-up, and even then, only for a fluid contained in the simplest computational domain, i.e. periodic in all three space directions. Second, identifying flow configurations that exhibit the specific route to chaos being targeted, among the several possible in multi-dimensional systems, is much more difficult in physically relevant problems than in engineered toy models with tunable parameters. Cascades sequentially doubling the period at every bifurcation may occur through mechanisms quite different from those leading to universality (e.g. Yanagida 1987; Kokubu, Komuro & Oka 1996; Homburg, Kokubu & Naudot 2001; Yalim, Welfert & Lopez 2019). Other routes to chaos are also common in fluid systems; in the Taylor–Couette system, for example, chaos has been found to arise following the Ruelle–Takens–Newhouse scenario (Swinney & Gollub 1985) or Shil’nikov-type bifurcations (Lopez & Marques 2005). All these difficulties justify why demonstrating Feigenbaum universality in a fluid system requires careful analysis.

1.3. *Accumulation point of the cascade and beyond*

The orbits of ever increasing period that arise in succession as the parameter is varied along the period-doubling cascade pile up at the accumulation point, beyond which chaotic dynamics ensues. Our interest extends also to phenomena occurring past this point. The existence of a reverse cascade, whereby chaotic bands successively merge in pairs as one moves away from the accumulation point, is a well-established property of simple model maps (Grossmann & Thomae 1977; Lorenz 1980). It is noteworthy that Huberman & Rudnick (1980) observed self-similarity in the numerical analysis of Lyapunov exponents at the onset of chaos. Nevertheless, the extent to which universality holds in the chaotic regime remains an elusive question. Libchaber (1983) tried to detect universality beyond the accumulation point in a natural convection experiment. To the authors’ knowledge, this is the first and only endeavour to unveil universality past the accumulation point of a period-doubling cascade in a fluid dynamics problem, but the results were rather crude due to experimental limitations. In theory, if universality holds beyond the accumulation point, the bifurcation diagram should be predictable, not only up to but also past this point, from the initial few period-doubling bifurcations. However, we have not been able to find any such attempts in the literature, even for low-dimensional models. While self-similarity of the reverse cascade past the accumulation point has been invariably observed and has been conjectured to hold universally, the underlying mechanisms remain unknown.

1.4. *Outline of the paper*

The paper is structured as follows. The problem formulation is presented in § 2, alongside a brief account of the numerical methods employed. Section 3 introduces the period-doubling cascade that is our object of study and illustrates the procedure by which period-doubling bifurcation points are accurately computed. The sequence of the first few such points is then exploited in § 4 to assess agreement with the first and second Feigenbaum constants and to extrapolate the expected occurrence of the accumulation point. A method for the detailed prediction of the bifurcation diagram in the neighbourhood of the accumulation point from just a few initial period-doubling bifurcations is devised in § 5. We further show how meaningful predictions can be made, in a statistical sense,

that extend beyond the accumulation point into the chaotic regime. Finally, the main findings are summarised and conclusions drawn in § 6.

2. Formulation of the problem

We consider an incompressible Newtonian fluid of kinematic viscosity ν , filling the gap between two infinitely long concentric rotating cylinders (figure 1a). The angular velocities of the inner and outer cylinders, of radii r_i^* and r_o^* , are denoted as Ω_i and Ω_o , respectively. A complete set of independent dimensionless physical parameters characterising the problem are the radius ratio $\eta = r_i^*/r_o^*$ and the two Reynolds numbers $R_i = dr_i^*\Omega_i/\nu$ and $R_o = dr_o^*\Omega_o/\nu$, where $d = r_o^* - r_i^*$ is the gap.

All variables are rendered dimensionless using d and d^2/ν as units for space and time, respectively. In cylindrical coordinates (r, θ, z) , the velocity $\mathbf{v} = (v_r, v_\theta, v_z) = v_r \hat{\mathbf{r}} + v_\theta \hat{\boldsymbol{\theta}} + v_z \hat{\mathbf{z}}$ and pressure p of the fluid are governed by the Navier–Stokes equations, the incompressibility condition and the zero axial net massflux condition, i.e.

$$\partial_t \mathbf{v} + (\mathbf{v} \cdot \nabla) \mathbf{v} = -\nabla p + \nabla^2 \mathbf{v} + f \hat{\mathbf{z}}, \quad (2.1)$$

$$\nabla \cdot \mathbf{v} = 0, \quad (2.2)$$

$$Q(\mathbf{v}) = \int_0^{2\pi} \int_{r_i}^{r_o} (\mathbf{v} \cdot \hat{\mathbf{z}}) r \, dr \, d\theta = 0, \quad (2.3)$$

where the axial forcing term $f = f(t)$ in (2.1) is instantaneously adjusted to fulfil the constraint imposed by (2.3). The no-slip boundary conditions at the cylinder walls are

$$\mathbf{v}(r_i, \theta, z) = (0, R_i, 0), \quad \mathbf{v}(r_o, \theta, z) = (0, R_o, 0), \quad (2.4)$$

with $r_i = r_i^*/d = \eta/(1 - \eta)$ and $r_o = r_o^*/d = 1/(1 - \eta)$. The base, laminar and steady circular Couette flow, henceforth referred to as CCF, has

$$\mathbf{v}_b = V_b \hat{\boldsymbol{\theta}} = \left(Ar + \frac{B}{r} \right) \hat{\boldsymbol{\theta}}, \quad p_b(r) = \int \frac{V_b^2}{r} \, dr, \quad f_b = 0, \quad (2.5)$$

with $A = (R_o - \eta R_i)/(1 + \eta)$ and $B = \eta(R_i - \eta R_o)/[(1 - \eta)(1 - \eta^2)]$. In what follows, we express the velocity and pressure fields as

$$\mathbf{v} = \mathbf{v}_b(r) + \mathbf{u}(r, \theta, z; t), \quad p = p_b(r) + q(r, \theta, z; t). \quad (2.6)$$

The fields q and $\mathbf{u} = u_r \hat{\mathbf{r}} + u_\theta \hat{\boldsymbol{\theta}} + u_z \hat{\mathbf{z}}$ are the deviations from the CCF solution. The nonlinear boundary value problem for \mathbf{u} and q is discretised using a solenoidal Petrov–Galerkin spectral scheme described by Meseguer *et al.* (2007). The unknown perturbation fields are approximated by means of a Chebyshev \times Fourier \times Fourier spectral expansion in (r, θ, z) , but in the annular-parallelogram domain $(r, \xi, \zeta) \in [r_i, r_o] \times [0, 2\pi] \times [0, 2\pi]$, where the 2π -periodicity is imposed in the transformed coordinates

$$\xi = n_1 \theta + k_1 z, \quad \zeta = n_2 \theta + k_2 z, \quad (2.7)$$

following Deguchi & Altmeyer (2013). Figure 2(a) shows the computational domain corresponding to $\eta = 0.883$ and the wavenumber set $(n_1, k_1, n_2, k_2) = (10, 2, 0, 4.5)$. The domain was specifically designed for the earliest onset of non-trivial solutions while keeping compatibility with the large-scale tilt of spiral turbulence. For this reason, the bifurcation scenario we investigate is fully compatible with the overall structure of intermittent patterns experimentally observed in the counter-rotating regime of the Taylor–Couette system and, at the same time, can be reasonably expected to precede any other

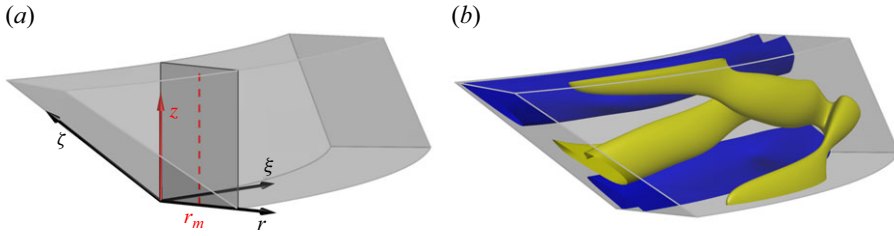


Figure 2. (a) Annular-parallel-gram computational domain defined by the coordinates of (2.7) with wavenumbers $(n_1, k_1, n_2, k_2) = (10, 2, 0, 4.5)$ and $\eta = 0.883$, adopted from W22. The axial line probe (red dashed vertical line) used in the production of space–time diagrams is located at mid gap $r_m = (r_i + r_o)/2 \approx 8.047$. (b) Three-dimensional flow structure of DRW solution for $(R_i, R_o) = (450, -1200)$. Positive (yellow, $u_\theta = 250$) and negative (blue, $u_\theta = -100$) isosurfaces of perturbation azimuthal velocity.

mechanism potentially leading to the onset of chaos. All computations have been run in this domain. The same resolution of $[0, 50] \times [-8, 8] \times [-8, 8]$ modes as used in W22 has been employed throughout. The system of ordinary differential equations that results from spatial discretisation has dimension $O(10^5)$.

To explore the dynamically relevant invariant sets, we combine direct numerical simulation (DNS) with a Poincaré–Newton–Krylov (PNK) iterative scheme. The spectrally discretised Navier–Stokes equations are integrated in time using a fourth-order linearly implicit IMEX scheme. The PNK scheme, built on top of the time integrator, looks for zeroes of a map defined with a purposely devised Poincaré section by means of a Krylov-space-based Newton solver. For a detailed account of the numerical methods used, refer to Ayats *et al.* (2020) and W22.

We characterise flow states by the normalised kinetic energy κ of the perturbation velocity field, and by the corresponding inner and outer cylinders normalised torque, τ_i and τ_o ,

$$\kappa = \frac{E(\mathbf{u})}{E(\mathbf{v}_b)}, \quad \tau_{i,o} = 1 + \left. \frac{\partial_r(r^{-1}\langle u_\theta \rangle_{\xi\zeta})}{\partial_r(r^{-1}V_b)} \right|_{r=r_{i,o}}, \quad (2.8)$$

where

$$E(\mathbf{v}) = \frac{1}{2\mathcal{V}} \iiint_{\mathcal{V}} \mathbf{v} \cdot \mathbf{v} \, d\mathcal{V} = \frac{1}{2\mathcal{V}} \int_0^{2\pi} \int_0^{2\pi} \int_{r_i}^{r_o} \mathbf{v} \cdot \mathbf{v} \, r \, dr \, d\xi \, d\zeta = \frac{1-\eta}{1+\eta} \int_{r_i}^{r_o} \langle \mathbf{v} \cdot \mathbf{v} \rangle_{\xi\zeta} \, r \, dr \quad (2.9)$$

is the volume-averaged kinetic energy of some velocity field \mathbf{v} . The volume of the transformed computational domain is $\mathcal{V} = 2\pi^2(r_o^2 - r_i^2) = 2\pi^2(1 - \eta)/(1 + \eta)$ and $\langle \cdot \rangle_{\xi\zeta}$ implies averaging in both parallelogram directions. With these definitions, $\kappa = 0$ and $\tau_i = \tau_o = 1$ for CCF.

The system possesses translational invariance in ξ and ζ . We define the entire set of possible spectral coefficients as the phase space. All coefficient vectors that belong to the group orbit induced by translation of a velocity field represent the same solution. We have systematically factored out the group orbit invariance employing the method of slices (Budanur *et al.* 2015), using the same template as Wang *et al.* (2023). To analyse the period-doubling cascade within the framework of discrete-time dynamical systems, we have devised a Poincaré section

$$\Sigma = \left\{ \mathbf{a} \in \mathbb{X} \mid \tau_i(\mathbf{a}) = \tau_o(\mathbf{a}), \frac{d\tau_i}{dt} > \frac{d\tau_o}{dt} \right\}, \quad (2.10)$$

in phase space \mathbb{X} , which consists of all possible sliced spectral expansion coefficients vector \mathbf{a} . The condition defining Σ is based on the equality of inner and outer cylinder torque (first condition), and the sign of the rate of change of their difference (second condition) to discard reverse crossings. It is easy to check from the governing equations that for statistically steady states, the time average of τ_i must coincide with that of τ_o . Consequently, long-lived (including permanent) time-dependent solutions are bound to regularly fulfil the condition $\tau_i = \tau_o$, a property that comes in handy in defining a robust Poincaré section. To simplify notation, we will hereafter call $\tau = \tau_i = \tau_o$ the value of the torque, whether inner or outer, on Σ .

There are other ways of sampling a continuous system to produce a discrete system. For example. Kreilos & Eckhardt (2012) and Gao *et al.* (2015) investigated the relationship between consecutive local maxima of the time series of some physical quantity. However, it is not easy to discern which minima/maxima are actually related to the underlying (pseudo-)periodicity of the solutions and which are simply incidental to the dynamics of the particular time signal used. Thus, the use of the above tailor-made Poincaré section provides a more reliable approach.

3. Period-doubling cascade

Emulating the influential experiments by Andereck *et al.* (1986), we employ a radius ratio $\eta = 0.883$ ($r \in [r_i, r_o] = [7.547, 8.547]$). The outer cylinder Reynolds number is fixed at $R_o = -1200$. For sufficiently large R_i , the centrifugal instability of the base flow develops into fully fledged turbulence. A reduction of R_i , while still in the supercritical region, has the flow re-organise into a pattern of alternating laminar and turbulent winding helical bands, commonly known as the spiral turbulence regime (Coles 1965; Andereck *et al.* 1986; Dong 2009; Meseguer *et al.* 2009b). At this particular value of R_o , the CCF is linearly stable for $R_i \lesssim 447.35$, but a number of subcritical nonlinear equilibrium states persist below this threshold (Meseguer *et al.* 2009a; Deguchi *et al.* 2014; and W22), which are believed to act as precursors of spiral turbulence. Drawing from the helix angle of the turbulent stripes observed experimentally, W22 employed the domain and coordinate system shown in figure 2(a) to seek minimal flow unit solutions that are compatible with the tilt of the banded pattern. Subharmonic instabilities of some such solutions were proposed as the mechanism that might be responsible for the spatial intermittency characterising spiral turbulence. Within this minimal parallelogram-annular periodic domain, which is capable of sustaining turbulence at sufficiently high R_i , W22 identified a stable finite amplitude travelling wave (shown in figure 2b) that coexists with the stable CCF. This drifting rotating wave, DRW for short, embodies all the essential elements of the self-sustaining mechanism (Wang, Gibson & Waleffe 2007; Hall & Sherwin 2010) and plays a central role in the transition process. In W22, two periodic solutions, P_1 , arising from a Hopf bifurcation of DRW, and P_2 , originating at a period-doubling bifurcation of P_1 , were also identified as the first steps in the route to chaos. This sequence of bifurcations suggested a period-doubling cascade as the most plausible scenario for the onset of chaotic dynamics, but the issue was not pursued further.

3.1. Onset of the period-doubling cascade

We now look into the bifurcation sequence the system undergoes in the range $R_i \in [395.43, 395.79]$ eventually leading to sustained chaotic dynamics. Since we will only be varying R_i , we shall drop the subscript and simply write R to ease notation.

Figure 3(a) shows the DRW (square), P_1 (dashed blue line) and P_2 (solid green line) at $R = 395.67$ in a three-dimensional projection of the full phase space \mathbb{X} on the subspace

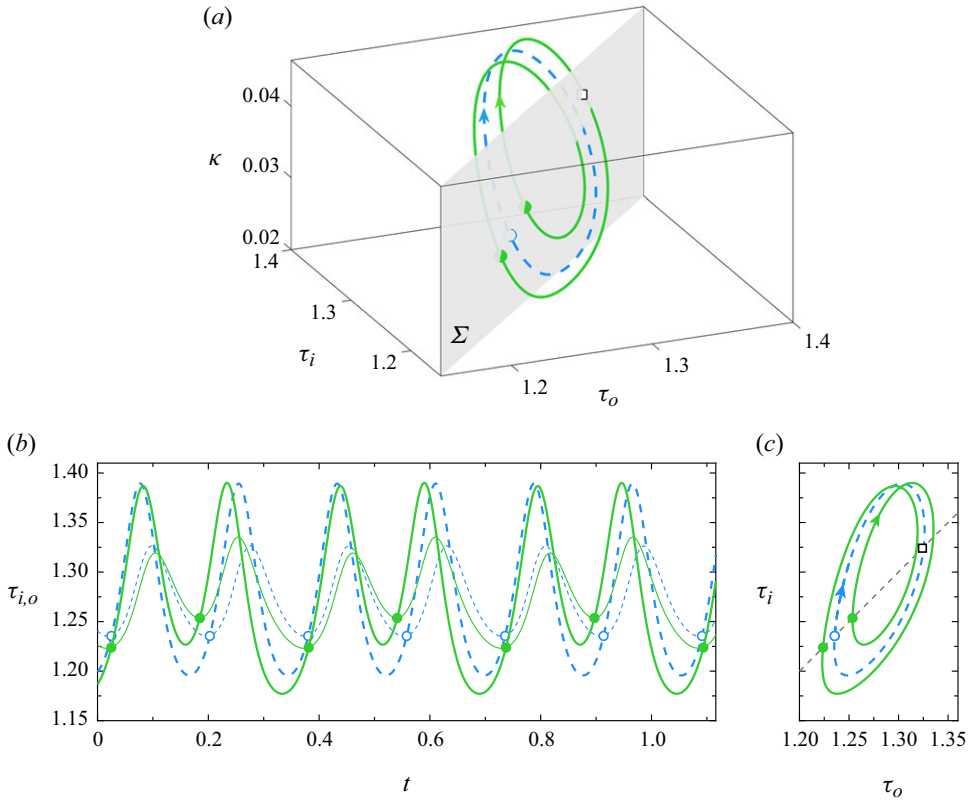


Figure 3. Poincaré section Σ and the periodic orbits P_1 (dashed blue) and P_2 (solid green). The black squares are DRW solutions. All solutions are computed at $R = 395.67$. (a) Projection of the phase space on the (τ_o, τ_i, κ) coordinates. (b) Inner (τ_i , thick lines) and outer (τ_o , thin) torque time series of P_1 and P_2 . (c) Two-dimensional phase map projection on the (τ_o, τ_i) plane. The Poincaré section is shown in transparent grey in panel (a) and as a dashed grey line in panel (c). The circles on the P_1 (empty blue) and P_2 (filled green) curves correspond to their representation on Σ .

spanned by the triplet of key quantities (τ_o, τ_i, κ) . The Poincaré section Σ appears in this representation as the transparent grey plane, which contains DRW and is pierced, in the direction defined by (2.10), at a single point by P_1 and at two different points by P_2 . In the torque time series of figure 3(b), the Poincaré crossings are conveniently identified as the intersections between the τ_i (thick lines) and τ_o (thin) signals for which the former is overtaking the latter. The two-dimensional projection of figure 3(a) onto the plane (τ_o, τ_i) , as depicted in figure 3(c), further clarifies how the sequence of intersection points of figure 3(b) collapses in phase space onto a single point for P_1 (empty blue disk) and as two distinct points for P_2 (filled green circles), all contained in Σ (dashed grey straight line).

The drift dynamics of non-axisymmetric solutions in Taylor–Couette as we have here is inevitably masked when monitoring aggregate quantities such as torque or kinetic energy due to their spatial averaging properties. Point measurements are instead subject to drift-induced time dependence. Figure 4(ai) presents a space–time diagram of the axial vorticity distribution measured along a line probe that is fixed in the lab reference frame (red dashed line in figure 2a). DRW, a relative equilibrium, is characterised by a solid-body motion composing axial translation and azimuthal rotation with constant phase velocities. As a result, the space–time diagram exhibits the repetition of a periodic pattern. The same line

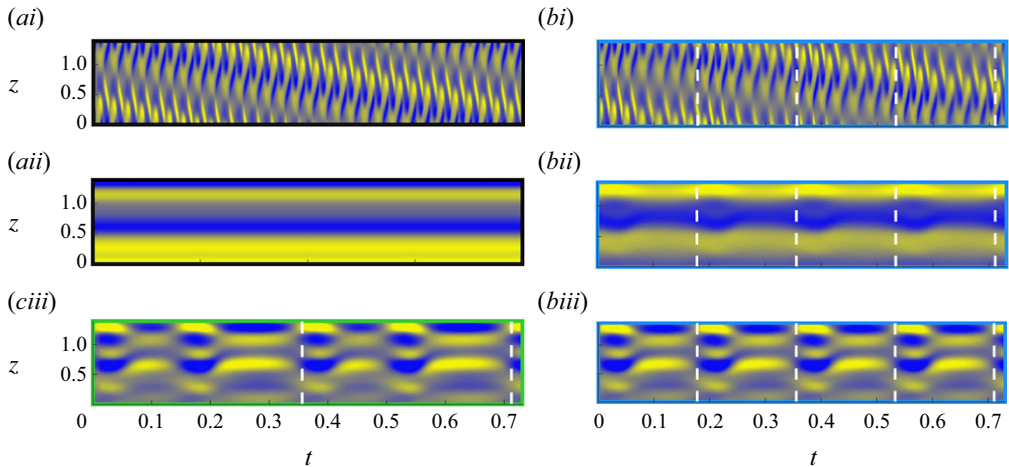


Figure 4. Space–time diagrams for (a) DRW, (b) P_1 and (c) P_2 , all computed at $R = 395.67$. The roman number labels denote measurements of radial vorticity $\omega_r(z; t)$ along axial probe lines at $(r, \theta) = (r_m, \theta_0)$ fixed to (i) the lab (stationary) reference frame, (ii) a reference frame co-moving with the solution and (iii) the same co-moving frame but with the temporal mean $\langle \omega_r \rangle_t$ subtracted. The azimuthal location, θ_0 , is chosen consistently across reference frames and solutions to enable comparison. Colour shading according to $\omega_r \in [-1400, 1400]$ or $\omega_r - \langle \omega_r \rangle_t \in [-300, 300]$, as need be. Dashed vertical lines indicate the natural period of the corresponding solution.

probe produces a quasi-periodic space–time diagram for P_1 , as shown in figure 4(bi). Here, P_1 is a relative periodic orbit and, therefore, requires suitable shifts in both the z and θ directions to align the flow fields after every one period to reveal the space–time invariance. The effects of the drift can be suppressed by attaching the line probe to a moving reference frame defined with the method of slices (Budanur *et al.* 2015; Wang *et al.* 2023). In this reference frame, the space–time diagrams of DRW and P_1 (figures 4a(ii) and 4b(ii)) are greatly simplified, the former appearing as time-independent and the latter as purely time-periodic.

Further subtraction of the time average helps expose the true nature of the time dependence of the solutions. For P_1 , the time-horizon considered in figure 4(biii) allows for just over four repetitions, as indicated by the dashed vertical lines. Solution P_2 , shown in figure 4(ciii), has instead a natural period about twice that of P_1 , the period-doubling consisting in a modulation that shortens one of the half-periods while lengthening the other.

Let us now shift our focus to the dependence of the solutions on the parameter R . Figure 5(a) shows the bifurcation sequence that DRW undergoes when varying the inner Reynolds number in the range $R \in [391.20, 395.90]$. DRW emerges from a saddle-node bifurcation (SN_1) at $R \simeq 391.50$ and, leaving aside subharmonic instabilities, the nodal (upper) branch (the one represented in figure 2b and the square in figure 3a, 3c) remains stable to perturbations fitting the domain until the advent of a supercritical Hopf bifurcation (H) at $R \simeq 392.85$. As reported by W22, this is the only known case of a stable non-trivial solution in the subcritical parameter regime of Taylor–Couette flow. Note that, here, we are only interested in the stability to perturbations that fit within the periodic box. Stable/unstable solutions are denoted by solid/dashed lines. The PNK method must be used to compute unstable solution branches. A stable relative periodic orbit (P_1 , blue line) bifurcates from DRW at H. All time-dependent solutions will be represented, from now on, through the collection of intersection points on the Poincaré section. The P_1 branch becomes unstable in a period-doubling bifurcation (PD_1), whence a branch of

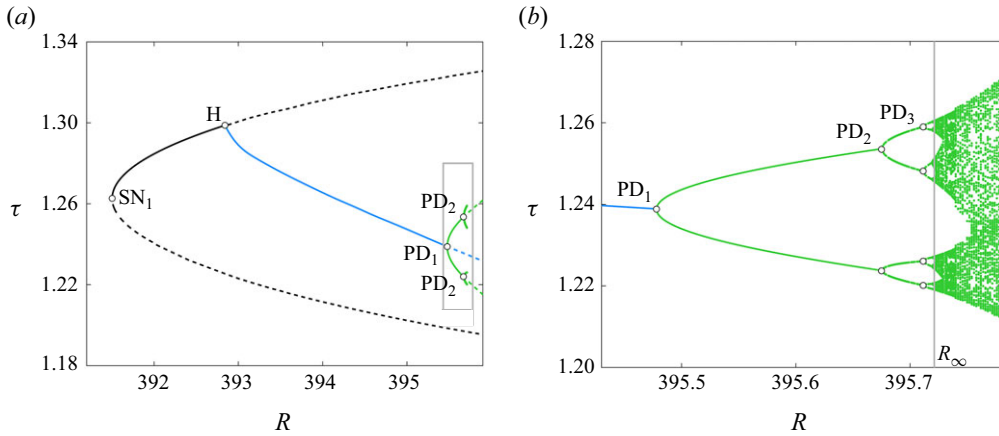


Figure 5. Bifurcation scenario as recorded on the Poincaré section Σ . (a) Initial steps of the bifurcation scenario. Shown are DRW (black), P_1 (blue) and P_2 (green), reported in W22. P_4 (green) emerges at the second period-doubling bifurcation point PD_2 . Both stable (solid line) and unstable (dashed) solution branches are shown. (b) Detailed view (close-up of the region bounded by a solid grey box in panel a) of stable solution branches across the period-doubling cascade and beyond. The accumulation point for the period-doubling cascade (R_∞) is to be computed in § 4.

stable period-doubled relative periodic orbits (P_2 , pair of green lines) emerges. The P_2 loses stability, in turn, in a second period-doubling bifurcation (PD_2) issuing a branch of period-4 solutions. The R value for which figures 3 and 4 were computed corresponds to just short of PD_2 , hence the instability of DRW and P_1 , in contrast with P_2 , which is stable.

The remainder of the period-doubling cascade and the onset of chaotic dynamics at larger values of R is depicted in figure 5(b). Only stable solutions are shown, so DNS is all that has been required to produce the solution branches in the diagram. Checking agreement with δ_F from the approximate location on the bifurcation diagram of the period-doubling points may seem a straightforward task. However, confirmation of Feigenbaum universality by brute force poses challenges, even for simple systems such as the logistic map. To begin with, the parameter spacing between consecutive period-doubling bifurcations shrinks very fast as one progresses along the cascade, demanding the computation of bifurcation points with an ever increasing number of significant digits. Moreover, the orbits in the immediate vicinity of a period-doubling point, which are required for the accurate estimation of the bifurcations, are close to neutrally stable and, therefore, take massive computational time to reach convergence with DNS. Unfortunately, employing the PNK method becomes impractical for solutions of increasingly long periods. The inability of the method to discriminate between stable and unstable orbits, combined with the fact that stable orbits in a period-doubling cascade coexist with all unstable orbits of lower period, which are favoured unless very close initial guesses are produced in advance, curbs any advantage one might have expected to achieve from using PNK. Both complications combined render the careful appraisal of agreement with Feigenbaum's first constant extremely hard. A rigorous and systematic analysis, as detailed in the coming section, becomes thus necessary.

3.2. Determination of period-doubling points

To analyse the period-doubling cascade, it is most convenient to focus on the sequence of \mathbf{a} on Σ . In the framework of dynamical systems theory, this corresponds to investigating the properties of the Poincaré map, also known as first return map. As we shall explain later,

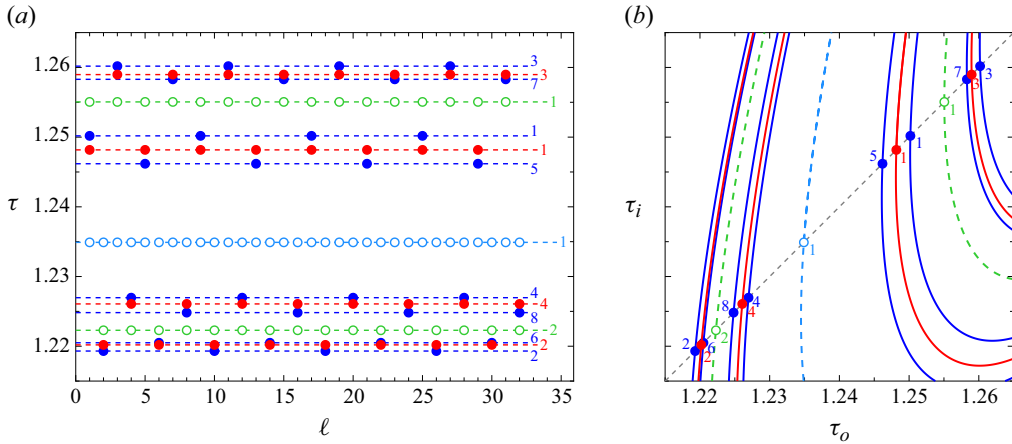


Figure 6. All orbits up to period 8 at $(P_1$ and P_2 , unstable) and around $(P_4$ and P_8 , at $R = 395.711$ and 395.719 , respectively) PD_3 . (a) Torque ($\tau = \tau_i = \tau_o$) of P_1 (cyan), P_2 (green), P_4 (blue) and P_8 (red) on Σ as a function of the discrete time ℓ (crossing index). The dashed lines indicate the distinct values of τ . (b) Two-dimensional phase map projection on the (τ_o, τ_i) plane. Shown are the phase map trajectories of all four orbits (dashed line for unstable, solid for stable) along with their representation on the Poincaré section (circles, open for unstable, filled for stable). The numbers indicate the order of the crossings.

it is not necessary to monitor the full set of coefficients, and the sequence of torque values provides (nearly) all necessary information in the long run, once the initial transients are over. Let $\tau(\ell)$, $\ell = 1, 2, 3, \dots$ be the corresponding sequence of torque values on Σ , with ℓ an index recording the chronological order. As an example, figure 6(a) shows $\tau(\ell)$ for the P_4 solution (red circles) at $R = 395.711$ (between PD_2 and PD_3) and for the P_8 solution (blue) at $R = 395.719$ (between PD_3 and PD_4). Both solutions are stable and well converged with DNS, such that the respective series sequentially repeat, always in the same order, the same four (P_4) and eight (P_8) distinct values, as indicated by the numbered horizontal dashed lines. The effect of the period-doubling bifurcation PD_3 can thus be portrayed as doubling point j of the P_4 discrete-time orbit into points j and $j + 4$ of the P_8 cycle, the latter two points having sprung from the former and drifted away in opposite directions. The unstable P_1 (cyan) and P_2 (green) orbits in the immediate vicinity of PD_3 are shown for reference, to help generalise the rule that relates points j and $j + N/2$ of the period- N orbit to point j of the period- $N/2$ orbit from which they bifurcate. A phase map analogous to that of figure 3(c) is shown in figure 6(b), but with the region where Σ is pierced by the orbits suitably magnified to further clarify where the P_4 and P_8 cycles stand in relation to P_1 and P_2 .

The n th period-doubling bifurcation PD_n can be readily analysed by splitting the $\tau(\ell)$ sequences of interest into $J = 2^n$ separate subsequences

$$\tau_j^J(k) = \tau(kJ + j), \tag{3.1}$$

each starting at one of J consecutive Poincaré crossings $j \in \{1, \dots, J\}$, and sampling every J th crossing thereafter. The limits

$$(\tau_j^J)_\infty = \lim_{k \rightarrow \infty} \tau_j^J(k) \quad j \in \{1, \dots, J\} \tag{3.2}$$

exist for all subsequences of all orbits of period $N = J = 2^n$ or lower ($J/2, J/4, \dots$) along the cascade, but fail for orbits of longer period ($2J, 4J, \dots$). Moreover, only period- J orbits will produce J distinct $(\tau_j^J)_\infty$ values, while shorter period orbits will have

the limits coincide in pairs according to $(\tau_j^J)_\infty = (\tau_{j+J/2}^J)_\infty$. This property is instrumental in telling apart orbits of period $N = J$ from orbits of period $J/2$ or smaller, as the amplitudes defined by

$$A_j^J = \left| (\tau_j^J)_\infty - (\tau_{j+J/2}^J)_\infty \right| \quad j \in \{1 \dots J/2\}, \quad (3.3)$$

will all vanish for any orbit other than P_J . For instance, suppose we slightly perturb the stable P_8 at $R = 395.719$. If we sample the τ sequence with $J = 8$, all subsequences $j = 1, 2, 3, \dots, 8$ converge and all eight limits are different (recall figure 6). Applying the same $J = 8$ sampling to a stable P_4 (or P_2 or P_1) will instead produce indistinguishable limits for j and $j + 4$ and, consequently, vanishing amplitudes $A_j^8 = 0$.

To nail down PD_3 , a collection of DNS runs traversing the bifurcation point, i.e. between $R = 395.711$ and 395.719 , are required. The amplitude of P_8 drops fast as the parameter R is decreased towards PD_3 , such that distinguishing it from P_4 becomes increasingly difficult. In addition, the dynamics become despairingly slow as the bifurcation point is approached from either side, rendering convergence with DNS downright impracticable. Figures 7(a) and 7(b) depict the torque subsequences at $R = 395.7116$ and $R = 395.7122$, respectively, below and above PD_3 but moderately close to the bifurcation point. Every pair of sequences $(\tau_j^8$ and τ_{j+4}^8 , depicted in different shades of the same colour) appears to be converging to the same value at $R = 395.7116$, but not at $R = 395.7122$. At these values of R , the achievable degree of convergence is still reasonable but sufficiently slow to illustrate how the estimation of the amplitudes may be systematised to parameter values much closer to the bifurcation point. Well past initial transients, and as the sequences approach convergence, the dynamics is progressively determined by the governing equations linearised around the stable solution. Therefore, we can expect that a power law fit of the form

$$\tau_j^J(k) = (\tau_j^J)_\infty + \left((\tau_j^J)_0 - (\tau_j^J)_\infty \right) (\lambda_j^J)^k, \quad (3.4)$$

with fitting parameters $(\tau_j^J)_\infty$, $(\tau_j^J)_0$ and λ_j^J , conforms reasonably well to the final transients. The fit provides an estimate for both the asymptotic torque value $(\tau_j^J)_\infty$ and the dominant multiplier λ_j^J . The dashed lines in the insets of the top panels of figure 7 are the fits to the sequences $\tau_j^J(k)$, $k \geq 0$. To expose the convergence rate and the accuracy of the fits, the same data have been plotted in the mid panels, now subtracting from each pair of branches j and $j + 4$ the mean value $((\tau_j^8)_\infty + (\tau_{j+4}^8)_\infty)/2$ at infinity. The fits provide an excellent approximation to the data points because the dynamics has already reached the linear regime. While all fitting curves decay to zero for $R = 395.7116$ in this representation, four distinct amplitudes arise for $R = 395.7122$. This unequivocally identifies the former dynamics as converging on a P_4 and the latter on a P_8 . The bottom panels plot the same data yet again, but now in logarithmic scale. In this representation, all fits to the individual torque subsequences are seen to collapse onto a single straight line. The eight slopes λ_j^8 , indistinguishable from one another to the naked eye, provide an estimate to the dominant multiplier of the converging periodic solution, interpreted as a P_8 regardless of its actual period.

The four amplitudes A_j^8 and eight multipliers λ_j^8 have been computed, following the same procedure with the sampling $J = 8$, at several values of R approaching PD_3 from either side, and plotted in figure 8. Figure 8(a) indicates that there is a well-defined critical value of R , beyond which, all four A_j^8 start growing following a square root law,

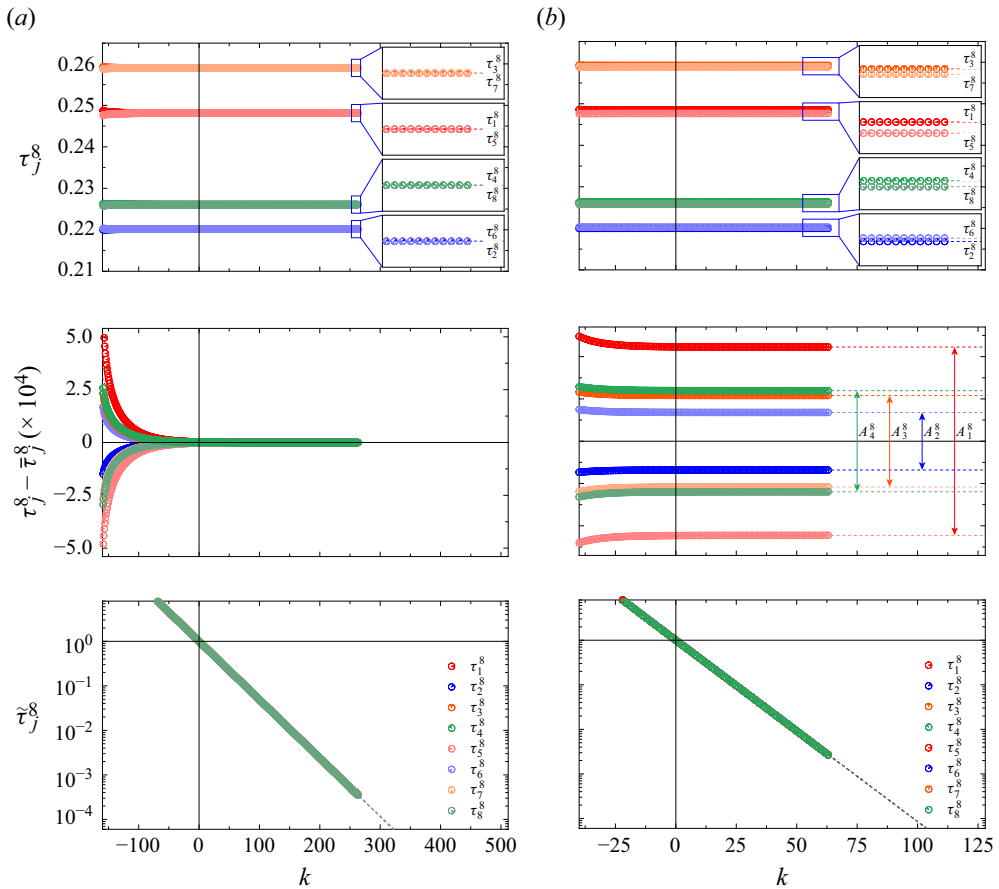


Figure 7. Analysis of torque sequences $\tau(\ell)$, sampled with $N = 8$ at (a) $R = 395.7116$ and (b) $R = 395.7122$, below and above PD_3 ($R = 395.711841564$, as we shall see later), respectively. The top panels show the eight sequences $\tau_j^8(k)$ (circles, magnified in the insets), alongside respective power law fits (dashed lines). To differentiate the eight subsequences, the points corresponding to each are coloured and represented with disks that are mainly blank except for a $1/8$ th sector, whose orientation ($360^\circ \times j/8$) uniquely identifies the corresponding sequence τ_j^8 (see the legend). The mid panels show the same data but with the mean value $\bar{\tau}_j^8 = [(\tau_j^8)_\infty + (\tau_{j+4}^8)_\infty]/2$ subtracted from every pair of branches to illustrate convergence. The bottom panels show again the same data but in logarithmic scale: $\tilde{\tau}_j^8 = [\tau_j^8 - (\tau_j^8)_\infty]/[(\tau_j^8)_0 - (\tau_j^8)_\infty]$.

as expected for a period-doubling bifurcation. To accurately pinpoint the critical value of the parameter for PD_n , a fit of the form

$$A_j^J(R) = a_j^J \sqrt{R - R_j^J} \tag{3.5}$$

with $J = 2^n$ applied to the first few points after the period-doubling bifurcation. The fits provide, besides the a_j^J values for the $J/2$ scaling factors, $J/2$ independent estimates R_j^J for the critical value of the parameter. A unique estimate for the critical value is then obtained by taking the arithmetic mean of the $J/2$ individual estimates as $R_n = \langle R_j^J \rangle$. Performing the $J/2 = 4$ fits to the data points of figure 8(a) (dashed lines), yields $R_3 = \langle R_j^8 \rangle = 395.71184156 \pm 5 \times 10^{-8}$ (violet square) for PD_3 .

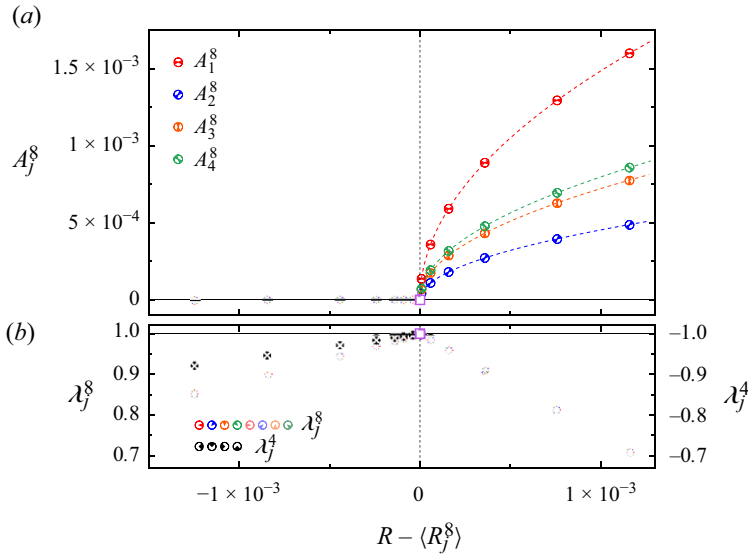


Figure 8. Analysis of PD₃. (a) Torque amplitudes A_j^8 and (b) multipliers λ_j^8 (coloured, sampling $\tau(\ell)$ with $N = 8$) and λ_j^4 (black, sampling with $N = 4$), as a function of inner cylinder Reynolds number $R - \langle R_j^8 \rangle$. The square-root fits are indicated with dashed lines. The lower bounds of the uncertainty of each point, shown as error bars, are sufficiently small to be imperceptible. Following the graphical representation of the τ_j^8 sequences of figure 7, each of the amplitudes is represented with a double-sectored disk that results from the superposition of the oppositely oriented sector disks of the two torques that define the amplitude, hence the hourglass appearance of the symbols.

The eight λ_j^8 multipliers, shown in figure 8(b), behave as expected across a period-doubling bifurcation. The eight individual fits (3.4) to the eight individual τ_j^8 subsequences produce nearly identical values of λ_j^8 at any given R , hence the multicoloured filled circles, resulting from the superposition of the eight oriented sector disks. The unique estimate of the multiplier at any given R , obtained as the arithmetic mean $\lambda_8 = \langle \lambda_j^8 \rangle$, increases towards unity as the period-doubling point is approached from either side. Since the solution above PD₃ is indeed a P₈, λ_8 is directly its multiplier. This is not so for the P₄ solution below PD₃. Plots analogous to those in figure 7(a) but sampling with $J = 4$ show that convergence onto the four asymptotic branches follows an oscillatory pattern. The multiplier of the P₄ orbit in the vicinity of PD₃ must be either computed from fits to the torque subsequences sampled with $J = 4$ or indirectly from λ_8 according to $\lambda_4 = \langle \lambda_j^4 \rangle = -\sqrt{\lambda_8}$. Either way, the multiplier of the stable P₄ in the vicinity of PD₃ is real, negative and on the way of leaving the unit circle of the complex plane through $\lambda = -1$ as R_3 is approached from below (black disks in figure 8b), consistent with the period-doubling nature of the bifurcation.

4. Verification of Feigenbaum universality

Signs that the period-doubling cascade may exhibit some sort of universality are already apparent from figure 9, where all orbits computed up to period $N = 128$ (past PD₇) are shown as a function of R . Successive magnifications, presented in figures 9(b) and 9(c), exhibit branch structures very similar to that of the full cascade of figure 9(a). Yet, at

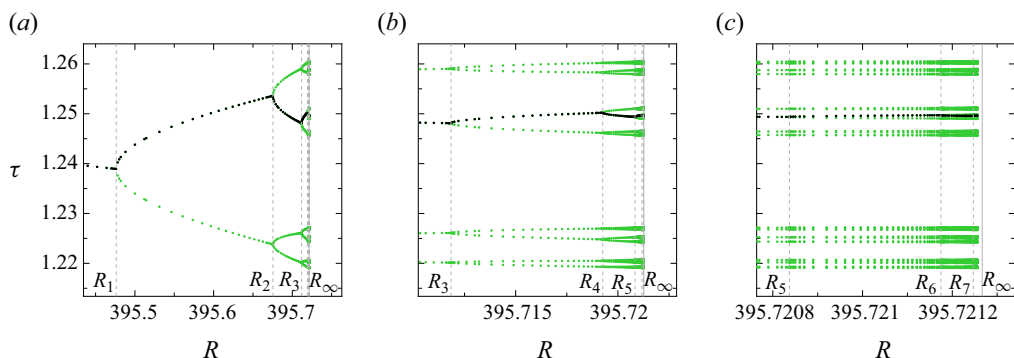


Figure 9. Successive magnifications of the period-doubling cascade. Same data as in figure 5(b), truncated at the accumulation point R_∞ , the central branch indicated with black dots. (a) Overview and (b,c) two successive levels of magnification. The first few period-doubling bifurcations (R_n , dashed) and the accumulation point (R_∞ , solid) are indicated with grey lines and labels.

this stage, there is no guarantee that the universality observed here is of the same kind as discovered by Feigenbaum.

To ascertain Feigenbaum universality, we have computed the sequence of critical R_n values along the period-doubling cascade up to order $n = 7$ to very high accuracy, using the method described in § 3.2. The results are summarised in table 2. For every $n \geq 3$, the table also lists the ratios δ_n , defined as

$$\delta_n = \frac{R_{n-1} - R_{n-2}}{R_n - R_{n-1}}, \tag{4.1}$$

which provide the best approximation to Feigenbaum’s first constant δ_F that may be obtained from data up to the n th period doubling. The trend of δ_n exhibits evident signs of conforming to Feigenbaum universality, that is, $\delta_n \rightarrow \delta_F$ as $n \rightarrow \infty$. It is instructive to compare these results with those in table 1. Limiting the analysis to $n = 4$, as customarily done in the fluid dynamics literature, does not guarantee convergence to even the second significant digit. Securing three digits precision is an arduous task that typically requires the accurate determination of at least $n = 7$ period-doubling bifurcation points.

The R_n sequence is expected to converge onto the accumulation point, $R = R_\infty$. This point may be computed by assuming that all period-doubling bifurcations of order higher than available are perfectly Feigenbaum-universal and, therefore, satisfy (4.1) with the left-hand side replaced by δ_F . However, this naive approach leads to systematic error. To obtain a better estimate of R_∞ and, at the same time, bound the error, we first note that

$$R_\infty = R_n + \sum_{m=n+1}^{\infty} \Delta R_m, \tag{4.2}$$

where $\Delta R_m \equiv R_m - R_{m-1}$ denotes the interval between the $(m - 1)$ and m th period-doubling bifurcations. Since (4.1) can be written as $\delta_n = \Delta R_{n-1} / \Delta R_n$, any successive m th interval may be expressed recursively in terms of previous intervals as

$$\Delta R_m = \delta_m^{-1} \Delta R_{m-1} = \delta_m^{-1} \delta_{m-1}^{-1} \Delta R_{m-2} = \dots = \delta_m^{-1} \delta_{m-1}^{-1} \dots \delta_{n+1}^{-1} \Delta R_n = \Delta R_n \prod_{\ell=n+1}^m \delta_\ell^{-1}. \tag{4.3}$$

n	$N = 2^n$	R_n		δ_n		α_n	
1	2	395.4762796241073	$\pm 6.9 \times 10^{-13}$	—	—	—	—
2	4	395.67542342	$\pm 5.3 \times 10^{-7}$	—	—	—	—
3	8	395.711841564	$\pm 4.2 \times 10^{-8}$	5.46826	$\pm 1.0 \times 10^{-4}$	-2.6668339	$\pm 8.1 \times 10^{-6}$
4	16	395.719257726	$\pm 8.7 \times 10^{-8}$	4.91065	$\pm 1.6 \times 10^{-4}$	-2.611741	$\pm 1.6 \times 10^{-5}$
5	32	395.72083697363	$\pm 2.9 \times 10^{-10}$	4.69601	$\pm 3.4 \times 10^{-4}$	-2.496646	$\pm 2.9 \times 10^{-5}$
6	64	395.7211746289	$\pm 4.7 \times 10^{-9}$	4.67710	$\pm 3.3 \times 10^{-4}$	-2.510893	$\pm 2.8 \times 10^{-5}$
7	128	395.7212469242	$\pm 1.4 \times 10^{-9}$	4.67050	$\pm 4.6 \times 10^{-4}$	-2.500577	$\pm 4.4 \times 10^{-5}$
...
∞	∞	395.721266624	$\pm 1.1 \times 10^{-8}$	4.66920160910299...	...	-2.50290787509589...	...

Table 2. Confirmation of Feigenbaum universality along the period-doubling cascade. The values of the critical inner cylinder Reynolds number R_n at the n th period doubling bifurcation point PD_n are used to compute the n th approximation, δ_n , to Feigenbaum’s first constant, according to (4.1). Approximations, α_n , to the second constant, are computed from central branch torque values following (4.8). Lower bounds to the uncertainties in the R_n , δ_n , α_n and R_∞ parameters have been rigorously estimated from the covariance matrices of the various fits involved in the process, combined with standard error propagation theory (note that we have not taken into account the error of the fit (3.4), as conducting a systematic study is difficult). The last row of the table corresponds to the accumulation point R_∞ estimated by (4.7), and the actual values of Feigenbaum constants, δ_F and α_F .

The accumulation point can then be formally expressed in terms of the n th period doubling and the immediately preceding interval as

$$R_\infty = R_n + \Delta R_n \left[\sum_{m=n+1}^{\infty} \prod_{\ell=n+1}^m \delta_\ell^{-1} \right]. \tag{4.4}$$

If $\delta_\ell = \tilde{\delta}_n > 1$ were constant for all $\ell > n$, then the terms in the square brackets would form a geometric series of sum $1/(\tilde{\delta}_n - 1)$. We conveniently define the average ratio beyond PD_n as

$$\tilde{\delta}_n = 1 + \left[\sum_{m=n+1}^{\infty} \prod_{\ell=n+1}^m \delta_\ell^{-1} \right]^{-1}, \tag{4.5}$$

so that (4.4) simplifies to

$$R_\infty = R_n + \frac{\Delta R_n}{\tilde{\delta}_n - 1} = \frac{\tilde{\delta}_n R_n - R_{n-1}}{\tilde{\delta}_n - 1}. \tag{4.6}$$

The constant $\tilde{\delta}_n$ is unknown and may only be estimated. For n sufficiently large, the sequence δ_ℓ for all $\ell > n$ is expected to approach δ_F monotonically from above. Under this assumption, inspection of (4.5) provides the inequalities $\delta_F < \delta_{n+1} < \tilde{\delta}_n < \delta_n$. Accordingly, upper and lower bounds for R_∞ can be obtained as

$$R_\infty \in \left[R_n + \frac{R_n - R_{n-1}}{\delta_n - 1}, R_n + \frac{R_n - R_{n-1}}{\delta_F - 1} \right], \tag{4.7}$$

by substituting $\tilde{\delta}_n = \delta_n$ and $\tilde{\delta}_n = \delta_F$ in (4.6), respectively. Using PD_7 , the upper and lower bounds for R_∞ are already within the uncertainty range of one another (see table 2) and, combined, provide an accurate estimate for the accumulation point $R_\infty = 395.721266624 \pm 1.1 \times 10^{-8}$.

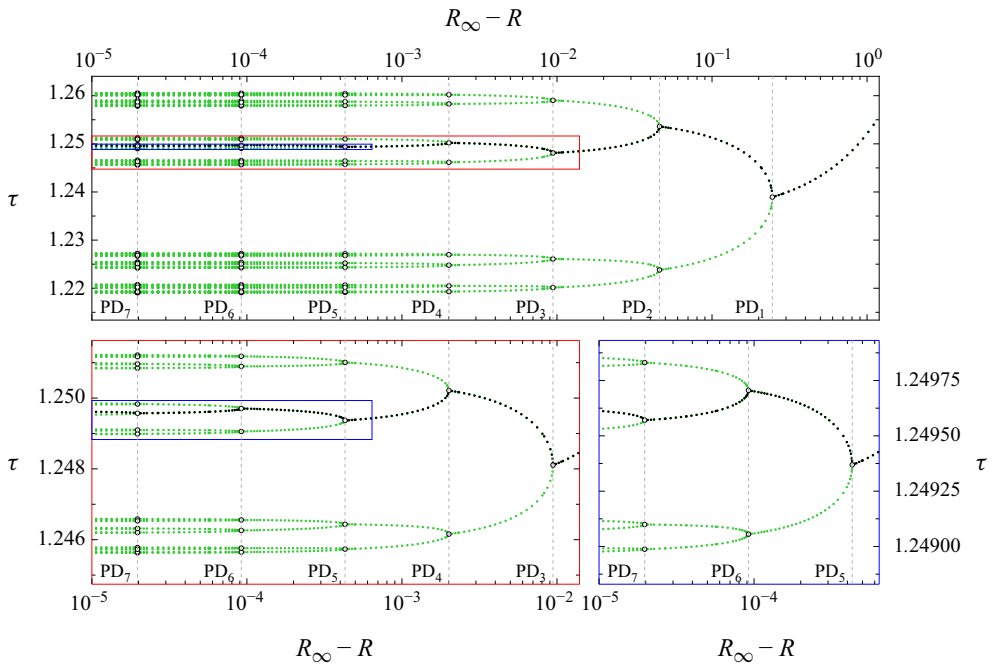


Figure 10. Self-similarity of the period-doubling cascade. Same data as figure 9 in log scale, the central branch represented with black dots. The coloured bottom panels are successive magnifications of the boxes in the top panel. The bifurcations are indicated with dashed vertical lines and labelled PD_n according to their order.

Following the determination of the accumulation point, we can now plot the period-doubling cascade as a function of $R_\infty - R$ in logarithmic scale (figure 10). The asymptotic approach to universality and the accuracy with which the accumulation point has been obtained are evident from the similarities observed after two consecutive magnifications of the period-doubling cascade (red and blue bottom panels).

The occurrence of Feigenbaum universality implies that the dynamics of the Navier–Stokes system is governed by a (nearly) one-dimensional discrete map. Figure 11(a) depicts a three-dimensional phase map projection of the orbit at the accumulation point R_∞ . If the manifold has dimension one, the coefficients \mathbf{a} on the Poincaré section Σ introduced in (2.10) can be uniquely parametrised by the torque, such that the first return map f defined by $\tau(\ell + 1) = f(\tau(\ell))$ contains all the long-term properties of the Poincaré map. The aperiodicity of the orbit becomes apparent when plotting $\tau(\ell + 1)$ as a function of $\tau(\ell)$ (green dots in figure 11b). The structure of the map on Σ is, however, not clear, as the Σ -crossings of the orbit are sparsely distributed (see figure 11a). Perturbing the orbit, dropping the first initial transients and plotting the remainder of the transients conveniently assists in populating the map more densely (black points). All the points thus obtained fall within a narrow, nearly one-dimensional band, seemingly connected by a smooth curve. This indicates that the discrete-time dynamics on Σ in the vicinity of the accumulation point can be well approximated by a one-dimensional map f . Note that, in the range of τ for which f appears to be multivalued (see the black points), the lower branch is never visited by the attractor and can, therefore, be ignored as regards its dynamics. Accordingly, the function f , with its leftmost branch duly trimmed, becomes unimodal and its smooth extremum (the minimum) admits a quadratic approximation. Note that unimodal maps

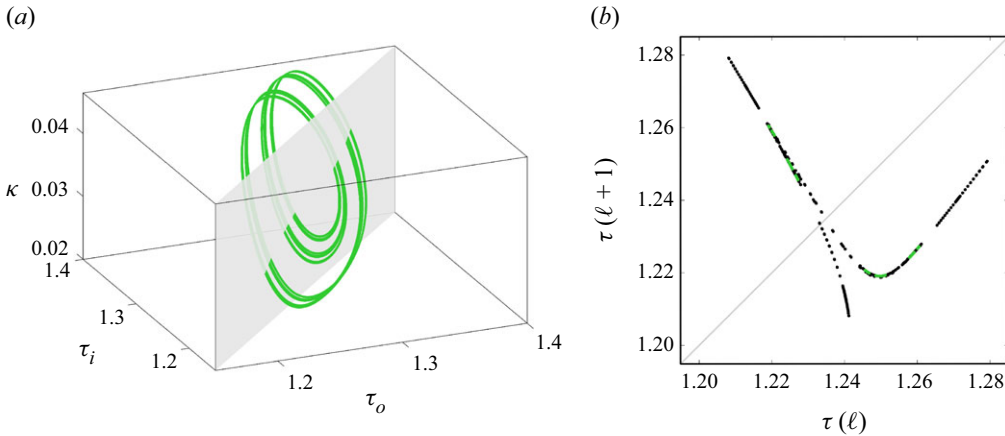


Figure 11. Phase portrait at R_∞ . (a) Three-dimensional phase map projection of the chaotic attractor. (b) First return iteration map on Σ populated by the chaotic attractor (green dots) and transients leading back to it following a perturbation (black).

with non-quadratic extrema provide universality constants that deviate from Feigenbaum’s well-known values (Briggs 1991).

For period-doubling cascades in one-dimensional unimodal maps, approximations of the second Feigenbaum constant, α_F , are often obtained from the central branch of the bifurcation diagram, which is generated by the periodic point that is nearest to the extremum of the map. Since producing accurate bifurcation diagrams of cascades undergone by fluid flow systems is an arduous task, Feigenbaum (1979) used instead the frequency spectrum, recorded at a fixed value of the parameter, of a natural convection experiment. In the subsequent studies summarised in table 1, no evaluation of agreement with α_F was conducted.

However, we have a highly accurate bifurcation diagram available, rendering direct assessment of agreement with the second constant possible. In the torque sequences presented so far, we have indexed the N distinct points visited by every periodic solution P_N as $j = 1, 2, \dots, N$ such that $j = 1$ is the central branch point (the black dots in figure 10). Thus, using the torque values of the central branch at PD_m , $\hat{\tau}_m = \tau_1^{2^m}(R_m)$, we can compute the ratios

$$\alpha_n = \frac{\hat{\tau}_{n-1} - \hat{\tau}_{n-2}}{\hat{\tau}_n - \hat{\tau}_{n-1}} \tag{4.8}$$

to be compared against the α_F appearing in the Feigenbaum–Cvitanović functional equation. The values of α_n thus obtained from the bifurcation diagram, listed in table 2 alongside δ_n , evidence gradual convergence toward Feigenbaum universality.

5. Prediction of the period-doubling route to chaos

Following the seminal work of Feigenbaum (1979), who showcased the first comparison with experimental results, Feigenbaum (1980, 1982, 1983) further extended renormalisation theory to include the universal scaling of all periodic points, not limited to the central branch, at different values of the parameter. The trajectory scaling function theory, which unravels the scaling between orbits featuring the same stability properties (i.e. having the same multiplier), was later applied to interpret experimental data on natural convection by Belmonte *et al.* (1988).

The occurrence of universality entails that, for any given unimodal map, one should be able to predict the entire structure of the bifurcation diagram near the accumulation point using data from only the initial few period-doubling bifurcations. Unfortunately, the trajectory scaling function method does not provide an easy way to predict the bifurcation cascade. Moreover, orbits become aperiodic beyond the accumulation point, hindering direct comparison with orbits at different parameter values. In this section, we devise a method for predicting the unfolding of the bifurcation cascade up to and beyond the accumulation point.

Consider a general one-dimensional discrete-time dynamical system described by

$$x_{\ell+1} = f_a(x_\ell). \tag{5.1}$$

We assume that the function $f_a(x)$ is unimodal and that a fixed point of the system (5.1) undergoes a period-doubling cascade as the parameter a is increased. In drawing parallels with our Navier–Stokes problem, we will later identify a and f_a with the Reynolds number R and the function approximating the return map of the torque sequence, respectively. Our claim, motivated by Feigenbaum (1982), is that the approximation

$$\frac{f_a^{2^n}(x) - X}{\gamma} \approx U_M^{2^n} \left(\frac{x - X}{\gamma} \right), \quad M = \frac{a - a_\infty}{\mu} \tag{5.2}$$

holds as long as 2^n is sufficiently large,

$$\left| \frac{\delta^n(a - a_\infty)}{\mu} \right| \ll 1, \quad \left| \frac{\alpha^n(x - X)}{\gamma} \right| < 1, \tag{5.3}$$

and provided the constants γ , X , μ and a_∞ are suitably chosen. The derivation of (5.2) and (5.3) is given in Appendix. To simplify the notation, we use functional powers to denote repeated application of a function (e.g. $f_a^2(x) = f_a(f_a(x))$). Also, we have dropped the F subscript when referring to Feigenbaum’s first (δ) and second (α) constants.

Here, the function U_M appearing in the approximation (5.2) is defined in terms of the Feigenbaum function G and the Feigenfunction Φ (with the normalisation $\Phi(0) = 1$) as

$$U_M(\xi) = G(\xi) + M\Phi(\xi). \tag{5.4}$$

The δ and Φ satisfy the eigenvalue problem $\mathcal{L}_G[\Phi] = \delta\Phi$. The precise form of the linear operator \mathcal{L}_G is given in Appendix. The nature of G and Φ is well understood (Collet & Eckmann 1980; Briggs 1991; Thurlby 2021). For our purposes, it will suffice to know that they are both smooth even functions, and that numerical recipes for their computation abound in the literature.

If the four (map-dependent) parameters, γ , X , μ and a_∞ , can be computed from the first few period doublings, then (5.2) provides a useful tool for predicting the behaviour of the dynamical system (5.1), subject to the constraints outlined by (5.3). In practice, fixing $n = 2$ and using data up to PD_{n+2} (i.e. PD_4) yields already reasonably accurate results. The procedure for prediction is straightforward, as we shall see shortly. All it takes is extracting template branches from the bifurcation diagram of the one-dimensional dynamical system

$$\xi_{\ell+1} = U_M(\xi_\ell), \tag{5.5}$$

and then stretch and translate them to align with corresponding branches of the bifurcation diagram of (5.1). The constants X and γ translate and scale the state x , while a_∞ and μ do the same for the parameter a . The constant a_∞ corresponds to the predicted accumulation point of the dynamical system (5.1). Thus, the first condition in (5.3) requires that the

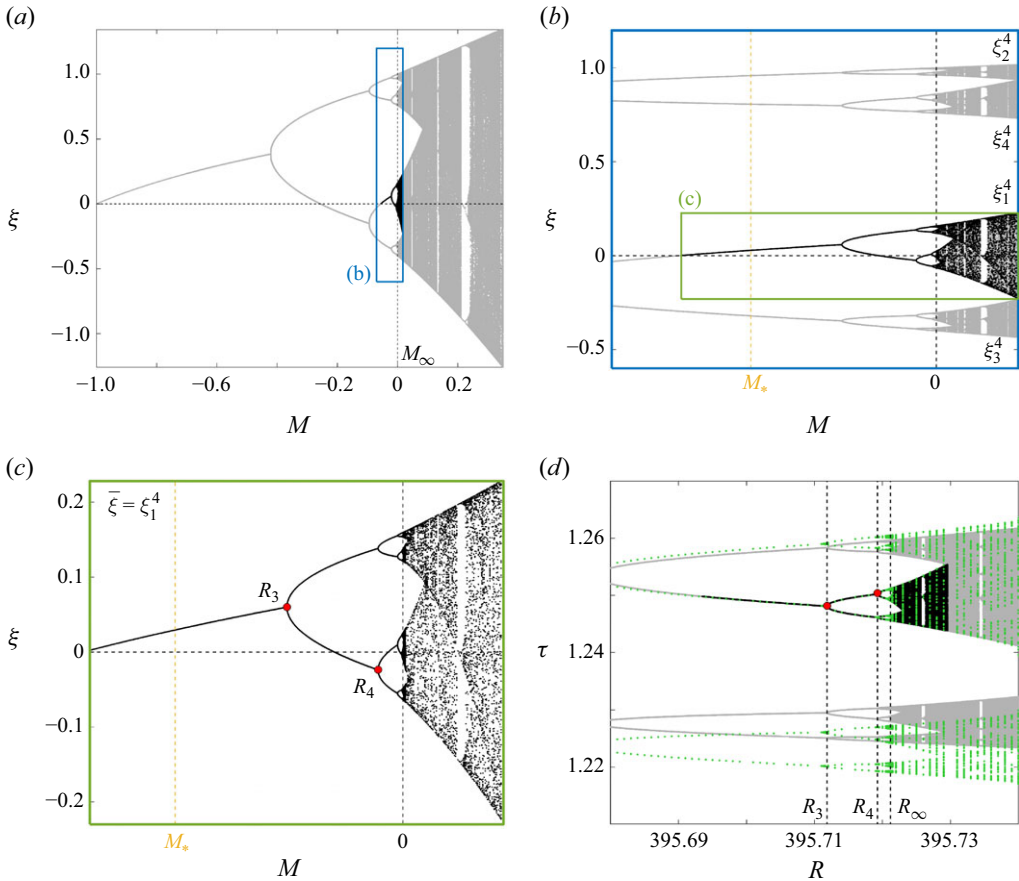


Figure 12. Bifurcation diagram of the one-dimensional map (5.5). (a) Full period-doubling cascade. (b) Magnification around the accumulation point M_∞ . The $2^n = 4$ distinct sets of points arising for $M > M_*$ are labelled as ξ_j^n , $j = 1, 2, 3, 4$. Black dots are used for the central branch, grey for the rest. (c) Close-up of the central branch $\bar{\xi} = \xi_1^n$. The red bullets at PD₃ and PD₄ are the points $(M, \xi) = (M_{n+1}, \hat{\xi}_{n+1})$ and $(M_{n+2}, \hat{\xi}_{n+2})$ selected for the matching with DNS data. (d) Full cascade transformed by (5.8) with $(\gamma, X, \mu, a_\infty)$ obtained by (5.7), compared with the period-doubling cascade in Taylor–Couette flow (green dots).

parameter a be sufficiently close to the accumulation point. Likewise, X corresponds to the predicted position of the extremum of the map $f_a(x)$ at $a = a_\infty$, and hence the second condition in (5.3) limits the validity of the approximation to a close neighbourhood of the extremum of the map $f_a(x)$, i.e. the central branch of the cascade. In brief, the conditions (5.3) imply that universality applies to the bifurcation diagram only locally. We will see later how the prediction can, nevertheless, be extended to the rest of the branches.

The bifurcation diagram of the dynamical system (5.5) is depicted in figure 12(a). It is easy to show that, for $M = -1$, the system has a stable fixed point at the origin ($\xi = 0$) and that $M = M_\infty = 0$ is the accumulation point of the period-doubling cascade. Assume that fixing the parameter M to a small (in modulus) negative value produces a stable orbit of, say, period $N = 2^n$ with $n \in \mathbb{N}$. An example of $M = M_*$ producing a period-4 orbit ($n = 2$) is shown in figure 12(b), which contains a magnification of figure 12(a) around the

accumulation point. Each of the 2^n branches at $M = M_*$ initiates its own period-doubling cascade as M is increased from M_* towards M_∞ . After the accumulation point, the 2^n distinct clouds of points induced by the 2^n separate branches start merging in pairs following a reverse cascade until eventually forming one sole object. We have labelled the four cascades as ξ_j^4 ($j = 1, 2, 3, 4$) in figure 12(b) and shown them up to the point where they first merge in two pairs (ξ_1^4 with ξ_3^4 and ξ_2^4 with ξ_4^4). We shall see that each of these cascade branches can act as a template in our prediction, but first, let us focus on the cascade induced by the central branch, henceforth denoted as $\bar{\xi} = \xi_1^4$ (see figure 12c).

To illustrate how the approximation (5.2) operates, we begin by fixing $M = M_*$ in figure 12(b), where we have an orbit of period $N = 2^n = 4$, so $n = 2$. Each template ξ_j^4 corresponds to a single point at this value of the parameter, with the j labels following the same sampling procedure of (3.1) with $J = 2^2$. Assuming that (5.2) is sufficiently accurate, we should be able to compare system (5.5) at $M = M_*$ with system (5.1) at $a_* = \mu M_* + a_\infty$. At $M = M_*$, the template solution $\bar{\xi}_* = \bar{\xi}(M_*)$ satisfies $U_{M_*}^{2^n}(\bar{\xi}_*) = \bar{\xi}_*$. Substituting $x = \bar{x}(a_*) = \bar{x}_* = \gamma \bar{\xi}_* + X$ into (5.2) yields $f_{a_*}^{2^n}(\bar{x}_*) \approx \bar{x}_*$, which implies that system (5.1) should exhibit a period- 2^n point well approximated by $x = \bar{x}_*$ at $a_* = \mu M_* + a_\infty$. This orbit should be stable because differentiation of (5.2) using $\xi = (x - X)/\gamma$ demands that

$$\frac{d}{dx} \left(f_{a_*}^{2^n} \right) \Big|_{x=\bar{x}_*} \approx \frac{d}{d\xi} \left(U_{M_*}^{2^n} \right) \Big|_{\xi=\bar{\xi}_*}, \tag{5.6}$$

which tells that the multiplier of the 2^n orbit of the map f_a must be reasonably well approximated by that of the universal map U_M . This result is actually not surprising because (5.2) indicates that the dynamics induced by the map $f_a^{2^n}(x)$ around $x = X$ are quantitatively similar to those induced by $U_M^{2^n}(\xi)$ around $\xi = 0$. The same argument can be made for the correspondence between solutions $\bar{\xi}(M)$ and $\bar{x}(a)$ at any $a = \mu M + a_\infty$, which need no longer be a single point as the central branch cascade unfolds. For $a \in (a_*, a_\infty)$, stable periodic orbits in the two systems can be related in the same way, and the approximate equality of multipliers follows from (5.6) analogously. Moreover, the dynamical similarity is not limited to periodic orbits, but applies also to aperiodic solutions for $a > a_\infty$. In general, we must interpret that the template solution $\bar{\xi} = \bar{\xi}(M)$ consists of a set of points satisfying $U_M^{2^n}(\xi_i) \in \bar{\xi}$ for all $\xi_i \in \bar{\xi}$ (i.e. the set is invariant under $U_M^{2^n}$). Then, (5.2) implies that the set $\bar{x}(a)$, defined as the collection of points $x_i = \gamma \xi_i + X$ for every $\xi_i \in \bar{\xi}(M)$, is invariant under $f_a^{2^n}$. Chaotic solutions related by $a = \mu M + a_\infty$ will have approximately the same Lyapunov exponents due to (5.6). All in all, the similarity of central branch dynamics between the two systems extends naturally all the way up to the accumulation point and beyond.

To find an adequate set of values for γ , X , μ , and a_∞ , one must pick two points in one of the bifurcation diagrams and find their analogues in the other. As a proof of concept, we select the first and second period-doubling bifurcation points that are encountered upon increasing M beyond M_* , where we have the stable period- 2^n orbit, namely PD_{n+1} and PD_{n+2} . We call the values of the parameter and of the central branch state variable $(M, \xi) = (M_{n+1}, \hat{\xi}_{n+1})$ and $(M_{n+2}, \hat{\xi}_{n+2})$ for PD_{n+1} and PD_{n+2} , respectively (see figure 12c). These same period-doubling bifurcation points are found to occur at $(a, x) = (a_{n+1}, \hat{x}_{n+1})$ and (a_{n+2}, \hat{x}_{n+2}) for the dynamical system (5.1), which, in the context of our DNS computations, correspond to $(R, \tau) = (R_{n+1}, \hat{\tau}_{n+1})$ and $(R_{n+2}, \hat{\tau}_{n+2})$ of § 4. The matching of both points from one bifurcation diagram to the other is accomplished by enforcing $M_m = (a_m - a_\infty)/\mu$ and $\hat{\xi}_m = (\hat{x}_m - X)/\gamma$ for $m = n + 1$

and $n + 2$. Solving the four resulting algebraic equations, we get

$$\begin{aligned}
 \gamma &= \frac{\hat{x}_{n+2} - \hat{x}_{n+1}}{\hat{\xi}_{n+2} - \hat{\xi}_{n+1}}, \\
 X &= \frac{\hat{\xi}_{n+2}\hat{x}_{n+1} - \hat{\xi}_{n+1}\hat{x}_{n+2}}{\hat{\xi}_{n+2} - \hat{\xi}_{n+1}}, \\
 \mu &= \frac{a_{n+2} - a_{n+1}}{M_{n+2} - M_{n+1}}, \\
 a_\infty &= \frac{M_{n+2}a_{n+1} - M_{n+1}a_{n+2}}{M_{n+2} - M_{n+1}}.
 \end{aligned}
 \tag{5.7}$$

If we set $n = 2$ and exploit the DNS results of [figure 10](#), the quadruplet of matching parameters takes the values $(\gamma, X, \mu, a_\infty) \approx (-0.02518, 0.2496, -0.4629, 395.7213)$. Finally, applying the transformation

$$\bar{x}(a) = \gamma \bar{\xi}(M) + X, \quad a = \mu M + a_\infty
 \tag{5.8}$$

to the full cascade generated by system (5.5) results in the branch arrangement shown in [figure 12\(d\)](#). The transformed cascade exhibits a remarkably good agreement with DNS for the central branch (black dots). However, the quality of the match does not carry over to the rest of the template branches. It is precisely in this sense that the approximation (5.2) is to be considered only local.

The prediction can, however, be straightforwardly extended to all 2^n branches of the cascade undergone by the system (5.1), by simply allowing for a different set of scaling and translation parameters for each of the branches. The transformation of the j th branch is performed according to

$$x_j^J(a) = \gamma_j \xi_j^J(M) + X_j, \quad a = \mu M + a_\infty, \quad j = 1, 2, 3, \dots, J,
 \tag{5.9}$$

where the pairs (γ_j, X_j) are obtained by matching the bifurcation points in the respective bifurcation diagrams, following the same procedure as for the central branch. The prediction thus obtained for the complete unfolding of the bifurcation cascade undergone by the DNS is shown in [figure 13](#). The agreement is now excellent for all four cascade branches. The success of the branch-by-branch matching process follows from the fact that the map $f_a^{2^n}(x)$ has $J = 2^n$ extrema, the approximation (5.2) being applicable to each individually. Note that, in the chaotic regime after the accumulation point, the dynamics of the two systems is not expected to match in detail due to the sensitivity to initial conditions. Nonetheless, the statistical properties should, in principle, be in fair agreement, as evidenced by [figure 13](#).

For simplicity, we have limited our comparison across systems to orbits of the same period. It is also possible to relate stable orbits of different periods, as Feigenbaum (1982) did, to demonstrate the self-similarity of the bifurcation diagram (see [Appendix](#)). Furthermore, our theoretical result is consistent with the fact that self-similarity also holds beyond the accumulation point, and that the Lyapunov exponent exhibits the scaling law observed by Huberman & Rudnick (1980). However, a detailed comparison of statistical quantities such as Lyapunov exponents is beyond the scope of our analysis, given that statistical convergence requires unaffordably long simulation times in the vicinity of the accumulation point (see Tirnakli, Tsallis & Beck 2009, for example). Instead, to gauge the accuracy of the prediction beyond the accumulation point, we have run DNS at a value of R for which the occurrence of a periodic window with a P_{12} orbit is anticipated. The time series of the Taylor–Couette system indeed appears to converge to a stable periodic orbit,

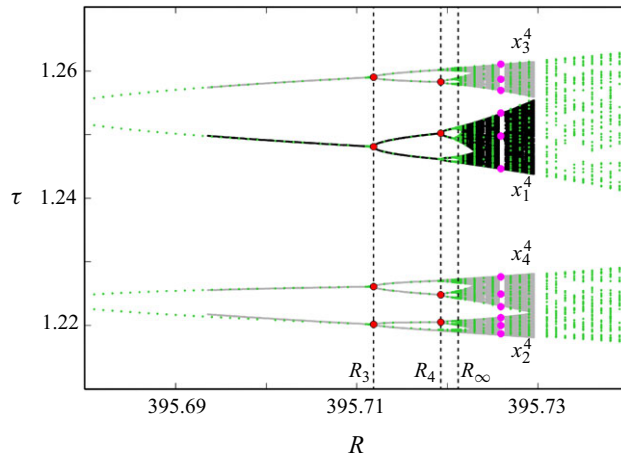


Figure 13. Branch-by-branch matching of period-doubling cascades. The black and grey points are the template branches shown in figure 12(b), re-adjusted according to the rescaling (5.9). The green points are the same DNS data as in figure 5(b). The matching process is based on the eight red points. The magenta points correspond to the P_{12} orbit in the Taylor–Couette system.

which we have confirmed to be the Navier–Stokes counterpart of P_{12} employing the PNK method (magenta dots in figure 13).

All self-similar features of the template period-doubling cascade should also show up in any cascade generated by a unimodal map. This implies that any other unimodal map, including the long-studied logistic map, could have been employed as a template. The advantage of the U_M defined in (5.4) stems from its natural emergence in the derivation of the approximation theory (as seen in Appendix), which grants very rapid convergence to universal dynamics by construction. Extending the prediction method to more general cases is straightforward using the results by Briggs (1991).

The core of our prediction method lies in completely separating the map-dependent scaling/translating parameters ($\mu, a_\infty, \gamma_j, X_j$) from all universality-related considerations. A careful reading of Feigenbaum’s work suggests that he was likely aware of this possibility. Notably, the method of trajectory scaling functions was specifically designed to eliminate all ingredients that depend on any particular map. However, to the authors’ knowledge, there is no direct assertion in the literature pointing at the feasibility of such predictions, let alone their applicability beyond the accumulation point.

6. Conclusions

We have studied in detail a period-doubling cascade that arises in subcritical counter-rotating Taylor–Couette flow employing small computational domains of annular-parallelogram shape. The cascade is seeded from a family of drifting rotating waves discovered by W22 and eventually leads to a chaotic regime fuelled by the self-sustained process of wall-bounded shear flows. Although the Navier–Stokes equations should formally be considered an infinite-dimensional dynamical system, the dynamics is often confined to finite-dimensional manifolds in phase space, sometimes designated as inertial manifolds (Temam 1989). This low dimensionality has recently attracted significant attention (Ding *et al.* 2016; Haller *et al.* 2023), as it affords valuable insight into the underlying dynamics of the flow, sometimes leading to simplified models whose numerical simulation is computationally more tractable. Our results can be interpreted as an extreme case of simplification that ultimately leads to a one-dimensional map representation.

A pivotal outcome of our analysis is the confirmation of Feigenbaum universality to an unprecedented degree of accuracy in the context of fluid dynamics. Our success is largely ascribable to the fast development of computational power over the past few decades, along with the outstanding numerical accuracy of the methods we employ to solve Navier–Stokes flows, which altogether has rendered thorough parameter sweeps feasible. That said, establishing universality has required very long and costly numerical simulations, a refined parametric exploration, and the deployment of very accurate numerical techniques for the detailed analysis of the asymptotic convergence of relative periodic orbits, the assessment of their stability and the computation of period-doubling bifurcation points. Determining both the first and second Feigenbaum constants to the third significant digit demands the precise computation of up to the seventh period-doubling bifurcation along the cascade. This has enabled an accurate estimation of the accumulation point and, with it, the unambiguous exposure of the self-similar structure of the period-doubling bifurcation cascade. A key element to make the analysis systematic has been the deployment of a convenient Poincaré section based on torque balance, which provides a robust sampling method to validate theories of unimodal discrete-time dynamical systems.

Furthermore, our results constitute the first confirmation of universality in a fluid flow problem subject to subcritical turbulent transition. A detailed study of period-doubling cascades is contingent on the existence and identification of a stable solution. In subcritical shear flows, stable solutions are rare and can only occasionally be found by working with minimal flow units and/or symmetry subspaces. We were fortunate enough to find one such solution in W22 that happens to be at the origin of a period-doubling cascade. It is also noteworthy that all solutions along the period doubling cascade exhibit spatial drift, a property that is unique to our system among the many previous studies on the subject (see [table 1](#)). As expected, the conventional Feigenbaum theory becomes applicable to the Taylor–Couette phase space once reduced by the method of slices (Budanur *et al.* 2015).

Drawing from Feigenbaum’s theory, we have further developed a method to predict the bifurcation diagram of the period-doubling cascade all the way up to the accumulation point and, remarkably, also beyond. This approach has broader applicability than the method of trajectory scaling functions (Feigenbaum 1983; Belmonte *et al.* 1988), which is limited to scrutinising stable orbits with the same value of the multiplier. Our prediction method is simple: it only requires stretching and shifting a template bifurcation diagram produced by any smooth unimodal map at hand. The scaling and translating parameters must be chosen such that the template bifurcation diagram aligns with the period-doubling cascade of the target system (in our case, Taylor–Couette flow). This can be accomplished, for example, by matching two bifurcation points across systems. The remainder of the transformed template diagram provides the prediction for the target system. The prediction results are useful, among other things, to anticipate the location of periodic windows in the bifurcation diagram of the target system beyond the accumulation point. The emergence of a stable orbit in the Taylor–Couette system precisely within the expected parameter range attests to the exceptional predictive capability of the method.

Our analysis further provides a theoretical explanation for the self-similarity that occurs in the reverse cascade following the accumulation point (see the Appendix). Since the theoretical result holds universally for unimodal maps, the excellent agreement between our DNS data and the reference one-dimensional map implies that self-similarity can be reasonably expected to extend beyond the accumulation point also for the Navier–Stokes system.

The observation of Feigenbaum universality in our Taylor–Couette set-up provides evidence that the dynamics around the accumulation point can indeed be approximated by a nearly one-dimensional discrete map when analysed on an appropriate Poincaré section.

Our finding further provides a handy playground for testing the application of iconic theorems from the early days of chaos theory, such as Li–Yorke or Sharkovsky’s (Sharkovskii 1964; Li & Yorke 1975), as well as cycle expansion theory (Cvitanović *et al.* 2016), to a fluid dynamics problem. It is our intention to explore the significance and implications of these theories to the field of fluid dynamics in the near future.

As briefly commented in § 1, understanding the laminar–turbulent pattern-formation aspects of subcritical transition using stochastic theories (Hof 2023) requires the prior occurrence of chaotic dynamics in the system. In shear flows, the incipient chaotic dynamics is only transient, such that the underlying chaotic saddle is not accessible through experiments or DNS. The scenario we have dissected offers a possible mechanism for the formation of one such chaotic saddle because our period-doubling cascade (i) occurs globally in the full annulus and (ii) is unstable to subharmonic (spatially modulational) perturbations, as can be inferred from W22. Both the full and elongated domains of figure 1(b) are simultaneously compatible with spiral turbulence and with the period-doubling cascade we address here. Evidence for property (ii) can indeed be drawn from W22, where the subharmonic instability of DRW, along with all solutions bifurcated from it in our small domain, was shown to contribute decisively to the formation of the laminar–turbulent helical pattern that is characteristic of the spiral turbulence regime. Therefore, although other mechanisms have been shown to produce localised chaotic sets that may be held responsible for intermittency in some cases (see Paranjape *et al.* 2023 for an example in channel flow), also a period-doubling cascade might work concurrently with a modulational instability to the same effect.

Funding. This research is supported by the Australian Research Council Discovery Project DP230102188 and the Ministerio de Ciencia, Innovación y Universidades (Agencia Estatal de Investigación, project nos. PID 2020–114043 GB-I00 (MCIN/AEI/10.13039/501100011033) and PID 2023–150029NB-I00 (MCIN/AEI/10.13039/501100011033/FEDER, UE). B.W.’s and R.A.’s research has been funded by the European Union’s Horizon 2020 research and innovation programme (Marie Skłodowska-Curie Grant Agreement No. 101034413). R.A. has also been funded by the Austrian Science Fund (FWF) 10.55776/ESP1481224.

Declaration of interests. The authors report no conflict of interest.

Appendix. Derivation of a universal approximation to a unimodal map and the conditions for validity

Consider the one-dimensional map (5.1), with $f_a(x)$ a unimodal function, undergoing a period-doubling cascade as the parameter a is increased. The location where the function has a maximum for $a = a_\infty$, the accumulation point, is denoted as $X = \operatorname{argmax} f_{a_\infty}(x)$. It will be convenient to shift the coordinate according to $y = x - X$ and define the shifted map as $F_a(y) = f_a(y + X) - X$.

If a is close to the accumulation point a_∞ , the function F_a may be approximated by a Taylor expansion truncated at first order, i.e.

$$F_a(y) \approx \Psi(y) + (a - a_\infty)\psi(y), \tag{A1}$$

where $\Psi = F_a|_{a=a_\infty}$ and $\psi = \partial_a F_a|_{a=a_\infty}$. Unimodal maps are known to be infinitely renormalisable at accumulation points (see Lanford III 1982, for example). Therefore, for large n and $a = a_\infty$, one must be able to find a function g , satisfying $\mathcal{R}[g] = g$, such that

$$\mathcal{R}^n[\Psi](y) \approx g(y). \tag{A2}$$

Note that $\gamma = g(0)$ is not necessarily unity and depends on the map f_a . The function g and the Feigenbaum function G introduced in § 1 are related by

$$G(\xi) = g(\gamma\xi)/\gamma. \tag{A3}$$

Next, we consider the Fréchet derivative of \mathcal{R} , in the direction of function $h(y)$, and evaluated at function $f(y)$:

$$\mathcal{L}_f[h](y) = \lim_{\epsilon \rightarrow 0} \frac{\mathcal{R}[f + \epsilon h](y) - \mathcal{R}[f](y)}{\epsilon} = \alpha h\left(f\left(\frac{y}{\alpha}\right)\right) + \alpha f'\left(f\left(\frac{y}{\alpha}\right)\right) h\left(\frac{y}{\alpha}\right). \tag{A4}$$

The operative expression of $\mathcal{L}_f[h](y)$ in terms of f and h is a well-known result (see Briggs 1991; Thurlby 2021, for example). The definition (A4), combined with the expansion (A1), implies $\mathcal{L}_\Psi[\psi] \approx (\mathcal{R}[F_a] - \mathcal{R}[\Psi])/(a - a_\infty)$, such that simple algebraic manipulation yields

$$\mathcal{R}[F_a] \approx \mathcal{R}[\Psi] + (a - a_\infty)\mathcal{L}_\Psi[\psi]. \tag{A5}$$

Moreover, it can be shown by induction that the n th renormalisation of F_a is given by

$$\mathcal{R}^n[F_a] \approx \mathcal{R}^n[\Psi] + (a - a_\infty)\mathcal{J}_n[\psi], \tag{A6}$$

where $\mathcal{J}_n = \mathcal{L}_{\mathcal{R}^{n-1}[\Psi]} \circ \mathcal{L}_{\mathcal{R}^{n-2}[\Psi]} \circ \dots \circ \mathcal{L}_{\mathcal{R}^0[\Psi]}$ and, of course, $\mathcal{R}^0[\Psi] = \Psi$. To deduce (A6), let us define $Q_k = \mathcal{R}^k[\Psi] + (a - a_\infty)\mathcal{J}_k[\psi]$. For $n = 1$, the statement (A6) reduces to $\mathcal{R}[F_a] \approx Q_1$, which is trivially satisfied in view of (A5). Now, assuming that $\mathcal{R}^k[F_a] \approx Q_k$ holds at step k , we just need to prove that $\mathcal{R}^{k+1}[F_a] \approx Q_{k+1}$ also holds. Using (A4), we get

$$\mathcal{J}_{k+1}[\psi] = \mathcal{L}_{\mathcal{R}^k[\Psi]}[\mathcal{J}_k[\psi]] \approx \frac{\mathcal{R}[\mathcal{R}^k[\Psi] + (a - a_\infty)\mathcal{J}_k[\psi]] - \mathcal{R}[\mathcal{R}^k[\Psi]]}{a - a_\infty}, \tag{A7}$$

which implies $\mathcal{R}[Q_k] \approx \mathcal{R}^{k+1}[\Psi] + (a - a_\infty)\mathcal{J}_{k+1}[\psi] = Q_{k+1}$. Operating \mathcal{R} on the induction step assumption yields $\mathcal{R}^{k+1}[F_a] \approx \mathcal{R}[Q_k] \approx Q_{k+1}$, which completes the proof of (A6).

The leading eigenvalue of the eigenvalue problem $\mathcal{L}_g[\varphi] = \delta\varphi$ is δ (i.e. Feigenbaum’s first constant) with associated eigenfunction φ . For sufficiently large n , the relation

$$\mathcal{J}_n[\psi] \approx \delta^n B\varphi, \tag{A8}$$

with B some constant, is expected to hold, because \mathcal{J}_n results from the repeated application, many times, of \mathcal{L}_g , which amplifies the most unstable mode. The eigenvalue problem can be recast in terms of the universal functions as $\mathcal{L}_G[\Phi] = \delta\Phi$, where

$$\Phi(\xi) = \mu B\varphi(\gamma\xi)/\gamma \tag{A9}$$

is normalised to $\Phi(0) = 1$ choosing the scaling factor appropriately as $\mu = \gamma/B\varphi(0)$.

Substituting (A2) and (A8) in (A6) yields

$$\mathcal{R}^n[F_a](y) \approx g(y) + (a - a_\infty)\delta^n B\varphi(y). \tag{A10}$$

Further replacing g and ϕ using (A3) and (A9), respectively, we obtain

$$\mathcal{R}^n[F_a](y) = \alpha^n F_a^{2^n}\left(\frac{y}{\alpha^n}\right) \approx \gamma \left\{ G\left(\frac{y}{\gamma}\right) + \delta^n (a - a_\infty)\mu^{-1}\Phi\left(\frac{y}{\gamma}\right) \right\}, \tag{A11}$$

where we have made explicit the effect of the renormalisation operator upon repeated application. To get back to the original map, we can use in (A11) the easily verifiable

proposition that repeated application of the original and shifted maps is related by $F_a^n(y) = f_a^n(y + X) - X$ for any $n \in \mathbb{N}$. Combined with the definition of the universal function (5.4), the approximation

$$f_a^{2^n}(x) \approx X + \Gamma_n U_M \left(\frac{x - X}{\Gamma_n} \right) \tag{A12}$$

follows directly, where the rescaled parameter M and magnification rate of the variable Γ_n have been defined as

$$M = \delta^n \mu^{-1} (a - a_\infty) \text{ and } \Gamma_n = \gamma / \alpha^n. \tag{A13}$$

Let us now consider what conditions are necessary for the approximation (A12) to be valid, besides the one requiring that 2^n must be large. The reliability of (A12) depends on the degree of trust one can place on the approximations (A2) and (A8). It is important to note that, in renormalisation theory, comparisons of functions are conducted on magnified scales. That is, while (A2) may be a good approximation on the scale where $y/\alpha^n = (x - X)/\alpha^n$ is not too large, it may not hold true on the original scale where $y \sim O(1)$ (mathematically, this can be easily understood by considering the case where Ψ is topologically conjugate to g). In (A12), it suffices to consider $U_M(\xi)$ with the argument in the range $\xi \in [-1, 1]$, which encompasses the entire period-doubling cascade of (5.5). Hence, the restriction $|(x - X)/\Gamma_n| < 1$, which makes (A2) only locally valid. The approximation (A8) is, again, local. Moreover, to use the approximation (A7) at level $k = n$, $|\delta^n (a - a_\infty)|$ must necessarily be small, so we require $|\delta^n M| \ll 1$.

The approximation (A12) must also hold for $U_M(\xi)$ itself, as it is unimodal in the range $\xi \in [-1, 1]$. We can therefore set $n = m$, $x = \tilde{x}$, $a = \tilde{M}$, $X = 0$, $a_\infty = 0$, $\mu = \tilde{\mu}$, $\gamma = \tilde{\gamma}$ and $f_a = U_{\tilde{M}}$ in (A12)–(A13) to obtain

$$U_{\tilde{M}}^{2^m}(\tilde{x}) \approx \tilde{\Gamma}_m U_M \left(\frac{\tilde{x}}{\tilde{\Gamma}_m} \right), \quad M = \delta^m \tilde{M} / \tilde{\mu}, \quad \tilde{\Gamma}_m = \tilde{\gamma} / \alpha^m, \tag{A14}$$

which should work as long as 2^m is large, $|\tilde{x}/\tilde{\Gamma}_m| < 1$ and $|\delta^m \tilde{M}| \ll 1$.

Finally, particularising (A12) for $n = \ell + m$, we get

$$\frac{f_a^{2^{\ell+m}}(x) - X}{\Gamma_{\ell+m}} \approx U_M \left(\frac{x - X}{\Gamma_{\ell+m}} \right) \approx \frac{\alpha^m}{\tilde{\gamma}} U_{\tilde{M}}^{2^m} \left(\frac{x - X}{\gamma \tilde{\Gamma}_\ell} \right), \tag{A15}$$

where the rightmost approximation is found by setting $\tilde{x} = (\tilde{\gamma}/\gamma)(x - X)\alpha^{-\ell}$ in (A14). The parameters a and \tilde{M} are linked by $\tilde{M} = \tilde{\mu}\delta^{-m}M = (\tilde{\mu}/\mu)\delta^\ell(a - a_\infty)$. We can simplify the notation by renaming $(\gamma/\tilde{\gamma})$ and $(\mu/\tilde{\mu})$ as γ and μ , respectively. In summary, the approximation

$$\frac{f_a^{2^{\ell+m}}(x) - X}{\Gamma_\ell} \approx U_M^{2^m} \left(\frac{x - X}{\Gamma_\ell} \right) \tag{A16}$$

is obtained if we redefine

$$M = \delta^\ell \mu^{-1} (a - a_\infty), \quad \Gamma_\ell = \gamma / \alpha^\ell. \tag{A17}$$

This approximation is valid for 2^m large, irrespective of the value of $\ell = 0, 1, 2, \dots$, as long as

$$\left| \frac{x - X}{\Gamma_{\ell+m}} \right| < 1, \quad |\delta^{\ell+m} \mu^{-1} (a - a_\infty)| \ll 1. \tag{A18}$$

The approximation (5.2) and conditions (5.3) quoted in the main text correspond to the case $\ell = 0$.

The self-similarity of the period-doubling cascade follows from the validity of the approximation (A16). Suppose we detect a period- 2^m stable orbit in (5.5) for M negative but close to zero. Then, the relation (A16) asserts the presence of period- $2^{\ell+m}$ orbits in (5.1) at $a = a_\ell = \delta^{-\ell} \mu M + a_\infty$ for every $\ell \in \mathbb{N}$. Moreover, the orbits must share the same multiplier, because an argument analogous to (5.6) can be applied.

The same self-similarity theory applies also to values of the parameter beyond the accumulation point. For instance, suppose we fix M at a small positive number so that a period $2^m p$ window is observed in (5.5), with p an odd number. Then, we can expect a period $2^{\ell+m} p$ window in (5.1) at $a_\ell = \delta^{-\ell} \mu M + a_\infty$ for every $\ell \in \mathbb{N}$. Even if the dynamics are predominantly chaotic, we can still expect similarity of the dynamics in the statistical sense. In particular, if $\lambda(M_*)$ is the Lyapunov exponent of (5.5) at $M = M_*$, the Lyapunov exponent of (5.1) at $a_\ell = \delta^{-\ell} \mu M_* + a_\infty$ should approximately be $2^{-\ell} \lambda(M_*)$. This is consistent with the observation by Huberman & Rudnick (1980). Note that this implies that for all unimodal maps, the distribution of Lyapunov exponents is identical immediately past the accumulation point.

REFERENCES

- ANDERECK, C.D., LIU, S.S. & SWINNEY, H.L. 1986 Flow regimes in a circular Couette system with independently rotating cylinders. *J. Fluid Mech.* **164**, 155–183.
- AYATS, R., DEGUCHI, K., MELLIBOVSKY, F. & MESEGUER, A. 2020 Fully nonlinear mode competition in magnetised Taylor–Couette flow. *J. Fluid Mech.* **897**, A14.
- BARKLEY, D. & TUCKERMAN, L.S. 2007 Mean flow of turbulent–laminar patterns in plane Couette flow. *J. Fluid Mech.* **576**, 109–137.
- BELMONTE, A.L., VINSON, M.J., GLAZIER, J.A., GUNARATNE, G.H. & KENNY, B.G. 1988 Trajectory scaling functions at the onset of chaos: experimental results. *Phys. Rev. Lett.* **61** (5), 539–542.
- BRIGGS, K. 1991 A precise calculation of the Feigenbaum constants. *Math. Comput.* **57** (195), 435–439.
- BUDANUR, N.B., CVITANOVIĆ, P., DAVIDCHACK, R.L. & SIMINOS, E. 2015 Reduction of SO(2) symmetry for spatially extended dynamical systems. *Phys. Rev. Lett.* **114** (8), 084102.
- BUZUG, TH, VON STAMM, J. & PFISTER, G. 1993 Characterization of period-doubling scenarios in Taylor–Couette flow. *Phys. Rev. E* **47** (2), 1054–1065.
- CHENG, L., JU, X., TONG, F. & AN, H. 2020 Transition to chaos through period doublings of a forced oscillating cylinder in steady current. *J. Fluid Mech.* **887**, A5.
- COLES, D. 1965 Transition in circular Couette flow. *J. Fluid Mech.* **21** (3), 385–425.
- COLLET, P. 2019 A short historical account of period doublings in the pre-renormalization era. *Comptes Rendus Mécanique* **347** (4), 287–293.
- COLLET, P. & ECKMANN, J.-P. 1980 *Iterated maps on the interval as dynamical systems*. Birkhäuser.
- COUGHLIN, K.T. & MARCUS, P.S. 1992 Modulated waves in Taylor–Couette flow part 2. Numerical simulation. *J. Fluid Mech.* **234**, 19–46.
- COULLET, P. & TRESSER, C. 1978 Iterations d'endomorphismes et groupe de renormalisation. *J. Physique IV (Proceedings) Le Journal de Physique IV* **39**, C5–25–C5–28.
- CVITANOVIĆ, P. 1989 *Universality in Chaos*. 2nd edn. Taylor & Francis.
- CVITANOVIĆ, P., RRUTUSO, R., MAINIERI, R., TANNER, G. & VATTAY, G. 2016 *Chaos: Classical and Quantum*. Niels Bohr Inst.
- DEGUCHI, K. & ALTMAYER, S. 2013 Fully nonlinear mode competitions of nearly bicritical spiral or Taylor vortices in Taylor–Couette flow. *Phys. Rev. E* **87** (4), 043017.
- DEGUCHI, K., MESEGUER, A. & MELLIBOVSKY, F. 2014 Subcritical equilibria in Taylor–Couette flow. *Phys. Rev. Lett.* **112** (18), 184502.
- DING, X., CHATÉ, H., CVITANOVIĆ, P., SIMINOS, E. & TAKEUCHI, K.A. 2016 Estimating the dimension of an inertial manifold from unstable periodic orbits. *Phys. Rev. Lett.* **117** (2), 024101.
- DONG, S. 2009 Evidence for internal structures of spiral turbulence. *Phys. Rev. E* **80** (6), 067301.
- ECKMANN, J.P. & WITTEBERG, P. 1987 A complete proof of the Feigenbaum conjectures. *J. Stat. Phys.* **46** (3–4), 455–475.
- EPSTEIN, H. 1986 New proofs of the existence of the Feigenbaum functions. *Commun. Math. Phys.* **106** (3), 395–426.

- FEIGENBAUM, M.J. 1978 Quantitative universality for a class of nonlinear transformations. *J. Stat. Phys.* **19** (1), 25–52.
- FEIGENBAUM, M.J. 1979 The onset spectrum of turbulence. *Phys. Lett. A* **74** (6), 375–378.
- FEIGENBAUM, M.J. 1980 The transition to aperiodic behavior in turbulent systems. *Commun. Math. Phys.* **77** (1), 65–86.
- FEIGENBAUM, M.J. 1982 Some formalism and predictions of the period-doubling onset of chaos. In *Nonlinear Problems: Present and Future*, (A. Bishop, D. Campbell & B. Nicolaenko), vol. 61, pp. 379–394. North-Holland.
- FEIGENBAUM, M.J. 1983 Universal behavior in nonlinear systems. *Physica D: Nonlinear Phenom.* **7** (1), 16–39.
- FELDMANN, D., BORRERO-ECHEVERRY, D., BURIN, M.J., AVILA, K. & AVILA, M. 2023 Routes to turbulence in Taylor–Couette flow. *Phil. Trans. R. Soc. Lond. A* **381** (2246), 20220114.
- GAO, Z., PODVIN, B., SERGENT, A. & XIN, S. 2015 Chaotic dynamics of a convection roll in a highly confined, vertical, differentially heated fluid layer. *Phys. Rev. E* **91** (1), 013006.
- GARCIA, F., SEILMAYER, M., GIESECKE, A. & STEFANI, F. 2021 Long term time dependent frequency analysis of chaotic waves in the weakly magnetized spherical Couette system. *Physica D: Nonlinear Phenom.* **418**, 132836.
- GIGLIO, M., MUSAZZI, S. & PERINI, U. 1981 Transition to chaotic behavior via a reproducible sequence of period-doubling bifurcations. *Phys. Rev. Lett.* **47** (4), 243–246.
- GLENDINNING, P. 1994 *Stability, Instability and Chaos: An Introduction to the Theory of Nonlinear Differential Equations*. Cambridge University Press.
- GROSSMANN, S. & THOMAE, S. 1977 Invariant distributions and stationary correlation functions of one-dimensional discrete processes. *Z. Naturforsch.* **32** (12), 1353–1363.
- HALL, P. & SHERWIN, S. 2010 Streamwise vortices in shear flows: harbingers of transition and the skeleton of coherent structures. *J. Fluid Mech.* **661**, 178–205.
- HALLER, G., KASZÁS, B., LIU, A. & AXÁS, J. 2023 Nonlinear model reduction to fractional and mixed-mode spectral submanifolds. *Chaos: Interdisciplinary J. Nonlinear Sci.* **33** (6), 063138.
- HAMILTON, J.M., KIM, J. & WALEFFE, F. 1995 Regeneration mechanisms of near-wall turbulence. *J. Fluid Mech.* **287**, 317–348.
- HOF, B. 2023 Directed percolation and the transition to turbulence. *Nat. Rev. Phys.* **5** (1), 62–72.
- HOMBURG, A.J., KOKUBU, H. & NAUDOT, V. 2001 Homoclinic-doubling cascades. *Arch. Rat. Mech. Anal.* **160** (3), 195–243.
- HUBERMAN, B.A. & RUDNICK, J. 1980 Scaling behavior of chaotic flows. *Phys. Rev. Lett.* **45** (3), 154–156.
- JIMÉNEZ, J. & MOIN, P. 1991 The minimal flow unit in near-wall turbulence. *J. Fluid Mech.* **225**, 213–240.
- KAWAHARA, G., UHLMANN, M. & VAN VEEN, L. 2012 The significance of simple invariant solutions in turbulent flows. *Annu. Rev. Fluid Mech.* **44** (1), 203–225.
- KHANIN, K., LYUBICH, M., SIGGIA, E.D. & SINAI, Y. 2021 Mitchell Feigenbaum. *Not. Am. Math. Soc.* **68** (5), 757–767.
- KOKUBU, H., KOMURO, M. & OKA, H. 1996 Multiple homoclinic bifurcations from orbit-flip I: successive homoclinic doublings. *Int. J. Bifurcation Chaos* **6** (05), 833–850.
- KREILOS, T. & ECKHARDT, B. 2012 Periodic orbits near onset of chaos in plane Couette flow. *Chaos* **22** (4), 047505.
- LANFORD III, O.E. 1982 A computer-assisted proof of the Feigenbaum conjectures. *Bull. Am. Math. Soc.* **6** (3), 427–435.
- LI, T.Y. & YORKE, J.A. 1975 Period three implies chaos. *Am. Math. Mon.* **82** (10), 985–992.
- LIBCHABER, A. 1983 Experimental aspects of the period doubling scenario. In *Dynamical System and Chaos*, (ed. L. GARRIDO), pp. 157–164. Springer.
- LIBCHABER, A. 2023 A journey through nonlinear dynamics: the case of temperature gradients. *Annu. Rev. Condens. Matter Phys.* **14** (1), 1–19.
- LIBCHABER, A., LAROCHE, C. & FAUVE, S. 1982 Period doubling cascade in mercury, a quantitative measurement. *J. Physique Lett.* **43** (7), 211–216.
- LIZÉE, A. & ALEXANDER, J.I.D. 1997 Chaotic thermovibrational flow in a laterally heated cavity. *Phys. Rev. E* **56** (4), 4152–4156.
- LOPEZ, J.M. & MARQUES, F. 2005 Finite aspect ratio Taylor–Couette flow: Shil’nikov dynamics of 2-tori. *Physica D: Nonlinear Phenom.* **211** (1–2), 168–191.
- LORENZ, E.N. 1980 Noisy periodicity and reverse bifurcation. *Ann. Lyceum of Nat. History of New York* **357**, 282–291.
- LUSTRO, J.R.T., KAWAHARA, G., VAN VEEN, L., SHIMIZU, M. & KOKUBU, H. 2019 The onset of transient turbulence in minimal plane Couette flow. *J. Fluid Mech.* **862**, R2.

- MARCUS, P.S. 1984 Simulation of Taylor-Couette flow. Part 2. Numerical results for wavy-vortex flow with one travelling wave. *J. Fluid Mech.* **146**, 65–113.
- MESEGUER, A., AVILA, M., MELLIBOVSKY, F. & MARQUES, F. 2007 Solenoidal spectral formulations for the computation of secondary flows in cylindrical and annular geometries. *Eur. Phys. J. Special Topics* **146** (1), 249–259.
- MESEGUER, A., MELLIBOVSKY, F., AVILA, M. & MARQUES, F. 2009a Families of subcritical spirals in highly counter-rotating Taylor-Couette flow. *Phys. Rev. E* **79** (3), 036309.
- MESEGUER, A., MELLIBOVSKY, F., AVILA, M. & MARQUES, F. 2009b Instability mechanisms and transition scenarios of spiral turbulence in Taylor-Couette flow. *Phys. Rev. E* **80** (4), 046315.
- MOORE, D.R., TOOMRE, J., KNOBLOCH, E. & WEISS, N.O. 1983 Period doubling and chaos in partial differential equations for thermosolutal convection. *Nature* **303** (5919), 663–667.
- PARANJAPE, C.S., YALNIZ, G., DUGUET, Y., BUDANUR, N.B. & HOF, B. 2023 Direct path from turbulence to time-periodic solutions. *Phys. Rev. Lett.* **131** (3), 034002.
- ROBERTS, E.P.L. & MACKLEY, M.R. 1996 The development of asymmetry and period doubling for oscillatory flow in baffled channels. *J. Fluid Mech.* **328**, 19–48.
- SCHUSTER, H.G. 1988 *Deterministic Chaos, An Introduction*. 2nd edn. VCH Publishers.
- SHAROVSKII, A.N. 1964 Co-existence of cycles of a continuous mapping of the line into itself. *Ukrainian Math. J.* **16**, 61–71.
- SMYRLIS, Y.S. & PAPANICOLAOU, D.T. 1991 Predicting chaos for infinite dimensional dynamical systems: the Kuramoto-Sivashinsky equation, a case study. *Proc. Natl Acad. Sci. USA* **88** (24), 11129–11132.
- STEPHENSON, J. & WANG, Y. 1991 Relationships between eigenfunctions associated with solutions of Feigenbaum's equation. *Appl. Maths Lett.* **4** (3), 53–56.
- STROGATZ, S.H. 2024 *Nonlinear Dynamics and Chaos - With Applications to Physics, Biology, Chemistry, and Engineering*. 3rd edn. Chapman and Hall/CRC.
- SWINNEY, H.L. & GOLLUB, J.P. 1985 Hydrodynamic instabilities and the transition to turbulence. In *Topics in Applied Physics*, vol. 45. Springer-Verlag.
- TEMAM, R. 1989 Do inertial manifolds apply to turbulence? *Physica D: Nonlinear Phenom.* **37** (1-3), 146–152.
- THURLBY, J.A. 2021 Rigorous calculations of renormalisation fixed points and attractors. PhD Thesis, University of Portsmouth, UK, Portsmouth.
- TIRNAKLI, U., TSALLIS, C. & BECK, C. 2009 Closer look at time averages of the logistic map at the edge of chaos. *Phys. Rev. E* **79** (5), 056209.
- TUCKERMAN, L.S., CHANTRY, M. & BARKLEY, D. 2020 Patterns in wall-bounded shear flows. *Annu. Rev. Fluid Mech.* **52** (1), 343–367.
- TUCKERMAN, L.S., KREILOS, T., SCHROBSDORFF, H., SCHNEIDER, T.M. & GIBSON, J.F. 2014 Turbulent-laminar patterns in plane Poiseuille flow. *Phys. Fluids* **26** (11), 114103.
- VAN VEEN, L. 2005 The quasi-periodic doubling cascade in the transition to weak turbulence. *Physica D: Nonlinear Phenom.* **210** (3-4), 249–261.
- WANG, B., AYATS, R., DEGUCHI, K., MELLIBOVSKY, F. & MESEGUER, A. 2022 Self-sustainment of coherent structures in counter-rotating Taylor-Couette flow. *J. Fluid Mech.* **951**, A21.
- WANG, B., MELLIBOVSKY, F., AYATS, R., DEGUCHI, K. & MESEGUER, A. 2023 Mean structure of the supercritical turbulent spiral in Taylor-Couette flow. *Phil. Trans. R. Soc. Lond. A: Math. Phys. Engng Sc.* **381** (2246), 20220112.
- WANG, J., GIBSON, J. & WALEFFE, F. 2007 Lower branch coherent states in shear flows: transition and control. *Phys. Rev. Lett.* **98** (20), 204501.
- YALIM, J., WELFERT, BRUNO D. & LOPEZ, J.M. 2019 Parametrically forced stably stratified cavity flow: complicated nonlinear dynamics near the onset of instability. *J. Fluid Mech.* **871**, 1067–1096.
- YANAGIDA, EIJI 1987 Branching of double pulse solutions from single pulse solutions in nerve axon equations. *J. Differ. Equ.* **66** (2), 243–262.